TU Delft

Delft University of Technology

Document Version
Final published version

Licence
CC BY

Citation (APA)
Hashimoto, Y., Masuda, R., Mulder, M., & van Paassen, M. M. (2026). A Human–Machine Interface for Efficient and Stable Blast Furnace Operation. *Metallurgical and Materials Transactions B: Process Metallurgy and Materials Processing Science*. https://doi.org/10.1007/s11663-026-04113-0

Important note
To cite this publication, please use the final published version (if applicable).
Please check the document version above.

Copyright
In case the licence states “Dutch Copyright Act (Article 25fa)”, this publication was made available Green Open Access via the TU Delft Institutional Repository pursuant to Dutch Copyright Act (Article 25fa, the Taverne amendment). This provision does not affect copyright ownership.
Unless copyright is transferred by contract or statute, it remains with the copyright holder.

Sharing and reuse
Other than for strictly personal use, it is not permitted to download, forward or distribute the text or part of it, without the consent of the author(s) and/or copyright holder(s), unless the work is under an open content license such as Creative Commons.

Takedown policy
Please contact us and provide details if you believe this document breaches copyrights.
We will remove access to the work immediately and investigate your claim.

This work is downloaded from Delft University of Technology.

ORIGINAL RESEARCH ARTICLE

A Human–Machine Interface for Efficient and Stable Blast Furnace Operation

YOSHINARI HASHIMOTO, RYOSUKE MASUDA, MAX MULDER, and MARINUS M. VAN PAASSEN

To achieve an efficient and stable operation of blast furnaces in the steel industry while retaining the proficient human operators' skills, a human–machine interface based on an ecological interface design (EID) was developed. EID is an interface design framework that reduces the cognitive workload of human operators by providing essential information on the controlled system in an intuitive way. The developed interface allows the operators to explore the possible control actions, by presenting the future predictions of the controlled variables when hypothetical control actions are taken, using a transient model. In addition, a graphical representation of the mass and energy balance that links the manipulated variables and controlled variables is provided to raise the situation awareness of the blast furnace operation. The developed interface is beneficial to determine appropriate control actions that maintain hot metal temperature and production rate near the target values and keep pressure drop below the upper bound while reducing carbon intensity and production costs.

https://doi.org/10.1007/s11663-026-04113-0
© The Author(s) 2026

I. INTRODUCTION

THE blast furnace (BF) process is the primary ironmaking process in the steel industry and is characterized by its superior thermal efficiency.[1,2] As of 2025, there are about 800 blast furnaces in the world, and over one billion tons of iron are produced annually by this process. Recent social demands for CO_2 reduction have encouraged BF operators to decrease the use of coke, which serves both as a reducing agent and as a spacer to ensure a stable gas flow. Low coke rate operation leads to unstable operations due to the lack of gas permeability. Hence, balancing highly efficient and stable operations has become more crucial.[3]

Figure 1 illustrates a schematic of a BF process with its typical geometry and size. It is a huge chemical reactor with a height of 40 m and a volume of 5000 m^3, producing about 10,000 tons of hot metal per day. In the blast furnace, layers of iron ore and coke are fed from the top of the furnace, and a hot blast at approximately 1200 °C is blown into the furnace through tuyeres at the lower part of the furnace. Auxiliary fuels, such as PC, are also injected from the tuyeres. The iron oxide in the iron ore is reduced by the carbon in the coke and PC, and the reduced iron is eventually melted to form liquid hot metal. The liquid hot metal and its byproduct, *i.e.*, slag, are drained from the bottom of the furnace at approximately 1500 °C.

The internal states of the BF process cannot be directly measured because it is extremely large and is operated under high-temperature conditions. Despite such adverse conditions, it is necessary to suppress the effects of large disturbances, such as fluctuations in the properties of the raw materials and gas flow.[4] Moreover, if a problem occurs in which the hot metal is chilled and solidifies in the furnace, it takes more than a month to recover. Accurate and timely control actions are mandatory to continue the efficient and stable operation.

Since the operation of the BF is difficult, it has conventionally relied on manual operation by human operators. In some actual furnaces, automatic control systems[5–7] and operation guidance systems[4,8] to stabilize the thermal status have been implemented. Simulation studies to validate the performance of control algorithms have been carried out.[3,9,10] However, full automation has not yet been achieved due to complicated phenomena that are extremely difficult to model accurately, *e.g.*, unburned PC generation,[11] raw

YOSHINARI HASHIMOTO is with the Cyber-Physical System R&D Department, Steel Research Laboratory, JFE Steel Corp., 1-1, Minamiwatarida-cho, Kawasaki 210-0855, Japan. Contact e-mail: y-hashimoto@jfe-steel.co.jp RYOSUKE MASUDA is with the Cyber-Physical System R&D Department, Steel Research Laboratory, JFE Steel Corp., 1, Kokan-cho, Fukuyama 721-8510, Japan. MAX MULDER and MARINUS M. VAN PAASSEN are with the Faculty of Aerospace Engineering, Delft University of Technology, 2629HS, Delft, The Netherlands.

Manuscript submitted March 28, 2026; accepted May 6, 2026.

Published online: 10 June 2026

material degradation,[12] and other powder-related phenomena. In addition, if the blast furnace, which is the dominant upstream process in a steel production site, stops operating, disruptions in the neighboring processes are unavoidable, resulting in significant economic losses. Therefore, promoting automation while keeping human operators in the control loop is considered the best way forward.

To help BF operators maintain situation awareness and keep them involved in the main decision-making loop, novel human–machine interfaces were investigated, adopting the ecological interface design (EID) framework.[13,14] EID supports the cognitive process of human operators by giving essential information on a controlled system in an intuitive way. For instance, a graphical representation of the mass and energy balance in a dual reservoir system was designed to help users better understand the links between the manipulated variables and controlled variables.[15] EID has shown to be effective in achieving operations where the human operators and machines work in coordination. While conventional control systems derive optimal actions by optimization algorithms, the ecological interface (EI) leaves the action decisions to the operators. Since the operators consider the possibility of various control actions on their own before executing them with the information provided by the system, efficient and stable operation can be achieved without compromising the operator's situation awareness and experience.

EID originates from the field of nuclear power plants,[16] and it has been widely applied in aviation automation,[17–19] process control,[20–22] and other safety-critical domains that are difficult to fully automate. The idea of EID has not been intensively applied to the blast furnace process, however. In this paper, we aim to develop an EI that allows the BF operators to derive the best control actions while understanding the internal mechanisms of the blast furnace process.

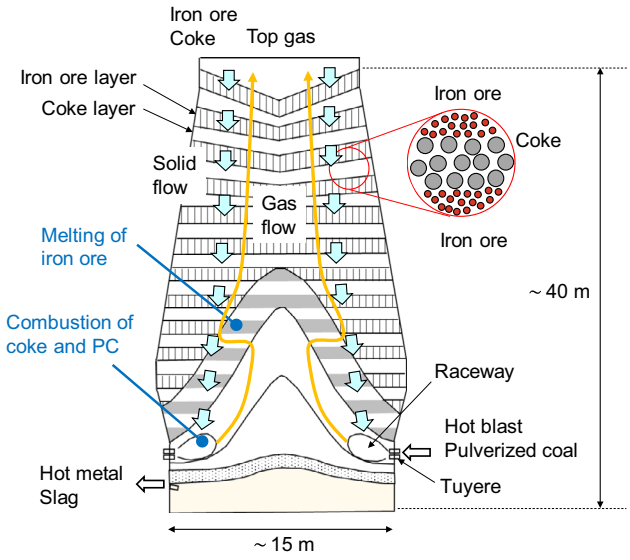

Fig. 1—Schematic of blast furnace process with its typical geometry and size.

The outline of this paper is as follows. Section II outlines the BF operation including the phenomena that take place in the BF and the relationship between the means and ends of the BF operation. Section III clarifies the internal process mechanism that links the means and ends from the perspective of mass and energy balance. Section IV develops the EI based on the process mechanism and presents an example of deriving the best control action using the developed EI. Section V summarizes this paper.

II. BLAST FURNACE OPERATION

This section provides an overview of the phenomena in the blast furnace that involve the mass and heat transport and the chemical reactions. The means and ends relationship to achieve the efficient and stable operation is then presented. Finally, an abstraction hierarchy analysis is conducted to identify the elements that need to be included in the EI.

A. *Phenomena in Blast Furnace Process*

Mass flow, *i.e.*, solid flow, liquid flow, and gas flow, forms the basis of the BF process as shown in Figure 1. The driving force of the solid flow is the consumption of solids that occurs in the lower part of the furnace. The coke is combusted by the oxygen in the hot blast supplied through the tuyeres. This combustion zone is referred to as the raceway after the swirling motion of the coke. The coke is also consumed by the direct reduction reaction and the dissolution of carbon into hot metal. The iron ore is completely melted in the lower part of the furnace, and the liquid hot metal and slag are drained from the bottom furnace. This consumption of the coke and the iron ore causes the solids to descend, and the coke and iron ore layers are fed alternately to maintain the surface height of the raw material. The driving force of the gas flow is the pressure drop (ΔP) between the tuyere and the top furnace. The coke layers have larger particles than the ore layers, and this is crucial to keep ΔP below the upper bound and obtain a stable gas flow.

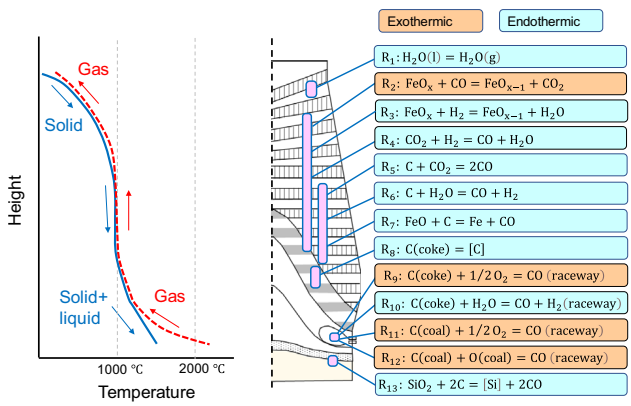

Fig. 2—Temperature distribution and chemical reactions inside BF.

Figure 2 shows the temperature distribution along the height direction. The chemical reactions inside the BF and the approximate height positions where they take place are also presented. The exothermic reactions and the endothermic reactions are highlighted in orange and light blue, respectively. The solids are charged at room temperature and heated up while descending through the furnace. In addition, the hot gas at around 2000 °C is formed in the raceway, which provides heat to the solids and liquids as it ascends through the BF. This raceway gas temperature is referred to as raceway adiabatic flame temperature (RAFT), and it is affected by the sensible heat of the hot blast, which is around 1200 °C, and the combustion heat of the coke and PC in the raceway.

In terms of chemical reactions, those related to the reduction of iron oxide by CO gas are explained here. CO gas is formed in the raceway mainly by the combustion of the carbon in coke and PC (R_9 and R_{11}). This formation of CO gas is comprised of two fast reactions: the generation of CO_2 by the complete combustion of coke and PC at the tip of the tuyere and the generation of CO by the reaction of this CO_2 with the solid carbon in the raceway. The CO gas is also generated by the direct reduction reaction (R_7) and the coke gasification reactions (R_5 and R_6) above 900 °C. The CO gas reduces the iron oxide while ascending in the furnace by the CO gas reduction reaction (R_2).

B. *Means and Ends in the BF Operation*

Figure 3 shows the means (manipulated variables) and ends (controlled variables) in the BF operation. The controlled variables are the hot metal temperature (HMT) at the furnace bottom, the production rate (Prod) defined by the iron loading rate from the furnace top, the pressure drop (ΔP), and the carbon intensity (I_C) per unit amount of iron. To control these variables, the coke rate (CR), the PC injection rate (PCI), and the blast volume (BV), *i.e.*, the flow rate of hot blast air, are

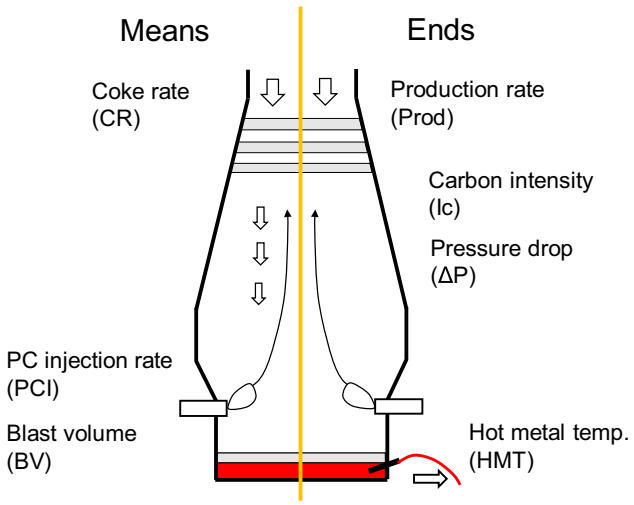

Fig. 3—Means and ends in BF operation.

Table I. Directions of Changes in Controlled Variables When Manipulated Variables are Increased

	Controlled Variables (Ends)			
Manipulated Variables (Means)	HMT	Prod	ΔP	I_C
BV	—	↑	↑	—
CR	↑	↓	↓	↑
PCI	↑	↓	—	↑

manipulated.[5] The directions of the changes in the controlled variables when the manipulated variables are increased are summarized in Table I.

In the BF operation, HMT must be kept constant.[23] If HMT is too low, slag viscosity increases, making the slag drainage difficult. On the contrary, if HMT is too high, excessive coke and PC are consumed, and the carbon intensity increases. HMT can be controlled by adjusting the PCI at the tuyere and CR at the top furnace. Increasing PCI increases HMT, but the HMT response is slow due to the large thermal inertia of the entire furnace, and the effect of the control actions only appears after about three hours of dead time.[24,25] When PCI cannot be manipulated due to operational constraints, CR is occasionally adjusted. In this case, the effect on HMT appears after the raw material descends to the tuyere level, resulting in a dead time of six to eight hours.[24,26]

The BF operation aims to achieve the target Prod demanded by the steelmaking process which adjusts the chemical components of the hot metal to produce steel. If the Prod does not reach the target value, economic losses will result. In contrast, if the Prod is excessive, the hot metal will need to be retained before the remainder of the steelmaking process, causing it to cool down. Additional energy is necessary to raise its temperature again to continue the steelmaking process. The Prod is approximately proportional to the hot blast flow rate (BV) supplied to the furnace. Increasing BV accelerates the coke consumption rate in the raceway and the material descent speed, leading to higher Prod.

Under the low CR operating conditions to reduce the carbon intensity and the production costs, the increase of ΔP becomes chronic.[27,28] High ΔP causes problems called gas channeling, where the hot gas blows up locally, making it very difficult to continue the stable operation. The hot gas that blows out can damage the furnace's top equipment, resulting in long-term shutdowns that occasionally last several months. High ΔP also disrupts the smooth descent of solids in the furnace, which is called hanging and slipping, and negatively affects the productivity. High ΔP may lead to the fluidization of fine particles in the raw material, which accompanies the increase of dust emitted from the top furnace and the loss of the raw material. Therefore, it is crucial to keep ΔP below an upper bound and stabilize the gas flow. Decreasing BV lowers the gas flow velocity and instantly decreases ΔP. Increasing CR to increase

the gas permeability is also effective in reducing ΔP, but its immediate effect is weak due to the traveling time of the material moving down.

As described above, the BF process must be operated so that the HMT and the Prod are close to the target values while ΔP does not exceed the upper bound. Furthermore, recent BF operations require a simultaneous reduction of PCI and CR to reduce the carbon intensity and production costs. The decrease of PCI and CR causes a drop in HMT, and the decrease of CR leads to the instability of the gas flow. The stable operation must be continued while meeting the requirements of reducing both the carbon intensity and production costs.

C. *Abstraction Hierarchy*

An ecological interface will be developed for the BF. To do so, an abstraction hierarchy (AH) analysis was conducted to clarify the hierarchical structure of the work domain.[13,29] The AH can identify the physical and chemical constraints involved in the work domain and the operational constraints in which the operators can take control actions.

The AH consists of five levels, and variables in the lower levels must be manipulated to achieve the state of the upper levels. The topmost level, *i.e.*, functional purpose, specifies the desired state of the entire process. The abstract function level describes the physical laws, such as the mass and energy balance, to realize the functional purpose. In the generalized function level, the specific processes that constitute each element at the abstract function level are shown. At the physical function level, the objects that compose the generalized function are described. Finally, at the physical form level, the appearance and location of each object at the physical function level are specified.

Figure 4 shows the AH of the blast furnace process. The functional purpose indicates the objective of the blast furnace process, that is, to produce the hot metal efficiently in a safe and stable manner. More specifically, the BF operation must meet the targets of Prod and HMT while minimizing the carbon intensity and keeping ΔP below the upper bound.

The abstract function shows the mass and energy balance required to achieve the functional purpose. In the BF, there are two types of mass and energy balance: the balance per second and the balance per iron.[30] The Prod is determined by the mass balance per second. ΔP is also roughly proportional to the gas flow rate and is therefore the outcome of mass balance per second. On the other hand, HMT and the carbon intensity are the amount of energy and carbon per unit amount of iron. Since the dynamics that govern the actual phenomena in the BF are based on the kinetics per second, the mass and energy balance per second is considered when decomposing it further into inputs and outputs.

The following generalized function level embodies the processes of mass and energy inputs and outputs. The mass inputs are iron and coke loading from the furnace top, PC, and hot blast injection from the tuyeres, whereas the mass outputs are the hot metal and slag drained from the bottom furnace and the top gas emission. The energy inputs consist mainly of the combustion heat of carbon at the raceway and the sensible heat of the hot blast. The dominant elements of the energy outputs are the sensible heat of hot metal and slag and the endothermic reaction heat, considering that most of the reactions above the tuyere level in Figure 2 are endothermic. The sensible heat of the top gas and the heat loss through the furnace wall also comprise the energy outputs. The physical function and physical form levels describe the physical objects and their locations that make up the generalized function.

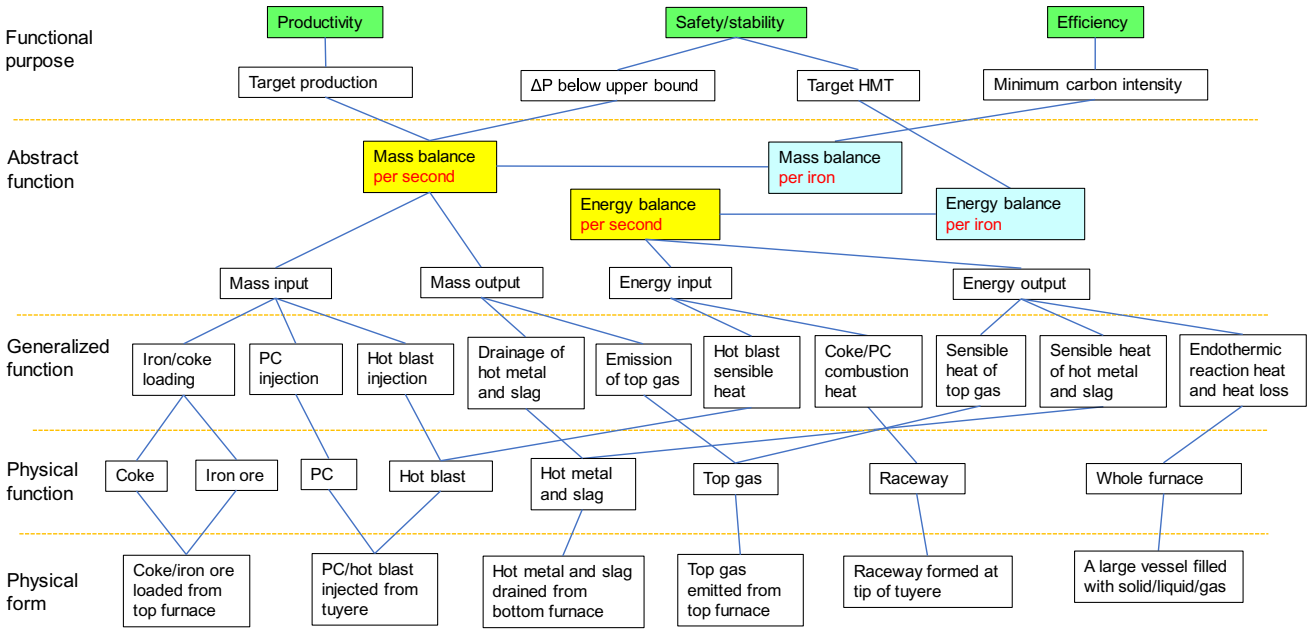

Fig. 4—Abstraction hierarchy of blast furnace.

Table II. Standard Operating Condition Used in Simulation

Input Variables	Value
Blast Volume (BV)	6,490 Nm^3/min
Enrichment Oxygen Rate (EO)	5.1 pct
Blast Moisture (BM)	31 g/Nm^3
Blast Temperature (BT)	1182 °C
Pulverized Coal Injection Rate (PCI)	595 g/Nm^3-O_2
Coke Rate (CR), *i.e.*, Weight Ratio of Coke and Iron	350 kg/t

The AH analysis indicates that the mass and energy balances are central in the BF operation. It is the manipulation of these balances within the operational constraints that should be conveyed to the operators.

III. MECHANISM THAT LINKS MEANS AND ENDS

In this section, a new graphical representation is developed to express the mechanism that links the means and ends of BF operation described in Section II-B. For this purpose, the elements that comprise the mass and energy balance described by AH in Section II-C are quantitatively specified. Conventional analyses regarding the mass and energy balance of the BF have focused on the operation improvements, such as the reduction of the carbon intensity, in steady-state conditions.[31–33] Since this study aims to control the dynamics of BF in real time, the mass and energy balance in transient states is visualized using a transient model.

A. *Transient Model of Blast Furnace*

The mass and energy balance inside the blast furnace is based on a one-dimensional (1D) transient model that has been previously developed and validated with real plant data.[24,25] This 1D transient model considers the 13 chemical reactions in Figure 2 and calculates the mass and heat transfer phenomena described in Section II-A. The four controlled variables in Table I are calculated by the six input variables: blast volume (BV), enrichment oxygen rate (EO), PC injection rate (PCI), blast moisture (BM), blast temperature (BT), and coke rate (CR). Of these six variables, BV, CR, and PCI are manipulated for control actions. In the real BF operation, however, BM and BT are also manipulated to control HMT. EO is occasionally manipulated to maintain RAFT when RAFT changes due to the manipulation of PCI, BM, and BT. In this work, to reduce the complexity of the interface and focus on the theoretical aspect of EID, BM, BT, and EO were kept constant.

The 1D transient model is represented by the following nonlinear state-space model:

$$\boldsymbol{x}(t+1) = f(\boldsymbol{x}(t), \boldsymbol{u}(t)) \quad [1]$$

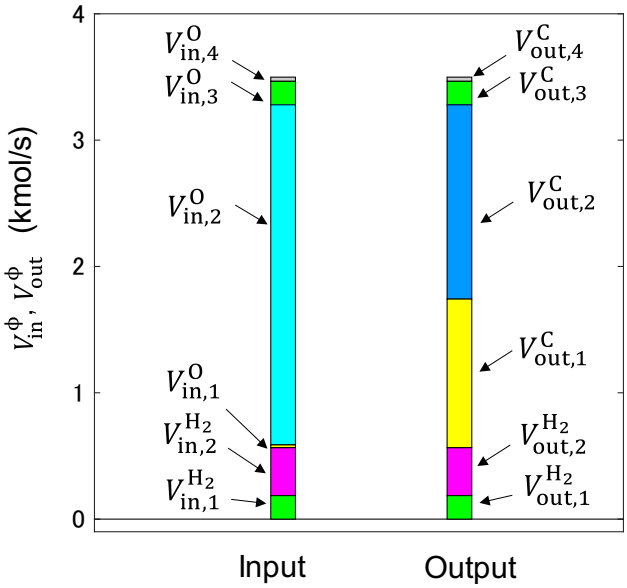

Fig. 5—Mass balance in lower furnace. Superscript ϕ in vertical axis denotes substances C, O, and H_2.

$$\boldsymbol{y}(t) = C(\boldsymbol{x}(t)) \quad [2]$$

where $\boldsymbol{x}(t)$, $\boldsymbol{u}(t)$, and $\boldsymbol{y}(t)$ are the state variables, input variables, and output variables at time step t, respectively. The nonlinear function f is obtained from the 1D transient model. The state variable $\boldsymbol{x}(t)$ represents the spatial distribution of the temperatures of gas, coke, and iron, the iron oxidation degree, and the hot metal composition in height direction. The input variables are denoted as $\boldsymbol{u}(t) = (BV(t), EO(t), PCI(t), BM(t), BT(t), CR(t))^T$. The function C calculates the output variables $\boldsymbol{y}(t) = (y_1(t), y_2(t), y_3 \quad (t), y_4(t))^T \equiv (Prod(t), I_C(t), HMT(t), \Delta P(t))^T$ from $\boldsymbol{x}(t)$. The time step of the nonlinear state-space model was set to 30 minutes considering the process dynamics and calculation time.

B. *Mass and Energy Balance*

This section organizes the mass and energy balance in the BF and explains how the controlled variables are determined from the manipulated variables. The calculation result at the steady state by the 1D transient model described in Section III-A under the standard operating condition in Table II is shown as an example.

1. *Mass Balance in the lower furnace*

This section describes the mechanisms by which CO and H_2 gases are formed in the lower furnace, *i.e.*, the raceway and the hearth region. Figure 5 shows the mass balance in the lower furnace. Table III describes the elements comprising mass and energy balance in Figure 5 and subsequent figures up to Figure 12. The column of the manipulated variable (MV) indicates that the element is directly affected by the manipulated variable, and that of the controlled variable (CV) indicates the

Table III. Elements of Mass and Energy Balance

Symbol	Variable	Unit	MV	CV	Figure No. 5	6	7	8	9	10	11	12
$V_{in,1}^{O}$	Oxygen flow rate contained in PC	kmol/s	*BV, PCI*		X			X	X			X
$V_{in,2}^{O}$	Oxygen flow rate in hot blast	kmol/s	*BV*		X			X	X			X
$V_{in,3}^{O}$	Oxygen flow rate in BM	kmol/s	*BV*		X			X	X			X
$V_{in,4}^{O}$	Oxygen reduction rate by R_{13}	kmol/s			X			X	X			X
$V_{in,1}^{H_2}$	Hydrogen flow rate contained in BM	kmol/s	*BV*		X			X	X			X
$V_{in,2}^{H_2}$	Hydrogen flow rate contained in PC	kmol/s	*BV, PCI*		X			X	X			X
V_{in}^{C}	Input rate of coke carbon	kmol/s				X	X	X	X			X
$V_{in}^{N_2}$	Nitrogen flow rate contained in hot blast	kmol/s	*BV*						X			X
V_{in}^{Fe}	Input rate of iron	kmol/s		*Prod*			X	X	X			X
$V_{out,1}^{C}$	Consumption rate of PC carbon	kmol/s	*BV, PCI*		X			X	X			X
$V_{out,2}^{C}$	Consumption rate of coke carbon by hot blast	kmol/s			X	X	X	XX	XX			XX
$V_{out,3}^{C}$	Consumption rate of coke carbon by BM	kmol/s			X	X	X	XX	XX			XX
$V_{out,4}^{C}$	Consumption rate of coke carbon by R_{13}	kmol/s			X	X	X	XX	XX			XX
$V_{out,5}^{C}$	Consumption rate of coke carbon by R_5, R_6, and R_7	kmol/s				X	X	X	X			X
$V_{out,6}^{C}$	Consumption rate of coke carbon by R_8	kmol/s				X	X	X	X			X
$V_{out,1}^{H_2}$	Hydrogen generation rate by BM	kmol/s	*BV*		X			X	X			X
$V_{out,2}^{H_2}$	Hydrogen generation rate by PC	kmol/s	*BV, PCI*		X			X	X			X
$V_{out}^{N_2}$	Nitrogen flow rate contained in top gas	kmol/s	*BV*						X			X
V_{out}^{Fe}	Melting rate of iron	kmol/s									X	X
I_{Coke}^{C}	Coke carbon intensity	kg/t	*CR*	I_C			X	X	X			X
I_{PC}^{C}	PC carbon intensity	kg/t		I_C				X	X			X
ΔP	Pressure drop	Pa		ΔP					X			X
$V_{in,1}^{E}$	Energy input rate by combustion of PC and coke	Mcal/s	*BV*							X	X	X
$V_{in,2}^{E}$	Energy input rate by R_2	Mcal/s								X	X	X
$V_{in,3}^{E}$	Energy input rate by sensible heat of N_2 contained in hot blast	Mcal/s	*BV*							X	X	X
$V_{out,1}^{E}$	Energy output rate by sensible heat of hot metal and slag	Mcal/s								X	X	X

Table III. continued

Symbol	Variable	Unit	MV	CV	Figure No. 5	6	7	8	9	10	11	12
$V^{E}_{out,2}$	Energy output rate by BM decomposition	Mcal/s								X	X	X
$V^{E}_{out,3}$	Energy output rate by R_5, R_6, and R_7	Mcal/s								X	X	X
$V^{E}_{out,4}$	Energy output rate by R_3	Mcal/s								X	X	X
$V^{E}_{out,5}$	Energy output rate by heat loss	Mcal/s								X	X	X
$V^{E}_{out,6}$	Energy output rate by other heats	Mcal/s								X	X	X
$I^{E}_{in,1}$	Energy input intensity by sensible heat of N_2 contained in hot blast	Mcal/t									X	X
$I^{E}_{in,2}$	Energy input intensity by R_2	Mcal/t									X	X
$I^{E}_{in,3}$	Energy input intensity by sensible heat of N_2 contained in hot blast	Mcal/t									X	X
$I^{E}_{out,1}$	Energy output intensity by sensible heat of hot metal and slag	Mcal/t		*HMT*							X	X
$I^{E}_{out,2}$	Energy output intensity by BM decomposition	Mcal/t									X	X
$I^{E}_{out,3}$	Energy output intensity by R_5, R_6, and R_7	Mcal/t									X	X
$I^{E}_{out,4}$	Energy output intensity by R_3	Mcal/t									X	X
$I^{E}_{out,5}$	Energy output intensity by heat loss	Mcal/t									X	X
$I^{E}_{out,6}$	Energy output intensity by other heats	Mcal/t									X	X

element directly linked to the controlled variable. Single X and double X in the right columns indicate that the element appears once and twice in the corresponding figure, respectively. The 12 elements in Figure 5 are marked by X in the column of Figure 5 in Table III.

The oxygen blown into the raceway consists of the oxygen content in the PC, the oxygen included in the hot blast and the enrichment oxygen (EO), and the oxygen in the BM. The respective input rates (kmol/s) at time step t are indicated as $V^{O}_{in,1}(t)$, $V^{O}_{in,2}(t)$, and $V^{O}_{in,3}(t)$:

$$V^{O}_{in,1}(t) = V^{PC}_{in}(t) \times X^{O}_{PC}/M_O/60 \quad [3]$$

$$V^{O}_{in,2}(t) = (BV(t) \times 0.21 + BVO(t))/22.4/60 \quad [4]$$

$$V^{O}_{in,3}(t) = (BV(t) + BVO(t)) \times BM(t)/M_{H_2O}/1,000/60 \quad [5]$$

where X^{O}_{PC} is the weight fraction of oxygen in PC, M_ϕ is the atomic weight or molecular weight of the substance ϕ, and $V^{PC}_{in}(t)$ is the PC flow rate (kg/min):

$$V^{PC}_{in}(t) = (BV(t) \times 0.21 + BVO(t)) \times PCI(t)/1,000/60 \quad [6]$$

$BVO(t)$ is the flow rate of EO added to the hot blast, which is determined by the input variables $BV(t)$ and $EO(t)$:

$$BVO(t) = BV(t) \times EO(t)/(79 - EO(t)) \quad [7]$$

All the oxygen blown into the raceway reacts with the carbon from coke or PC and is converted to CO gas. The reactions between the carbon and the oxygen in the raceway are $R_i (i = 9, 10, 11, 12)$ in Figure 2. Let $V^{C}_{out,1}(t) = R_{11} + R_{12}$ be the consumption rate of the carbon in the PC, $V^{C}_{out,2}(t) = R_9$ be the consumption rate of the coke carbon by the oxygen included in the hot blast and EO, and $V^{C}_{out,3}(t) = R_{10}$ be the consumption rate of the coke carbon by the BM. Since the molar ratio of carbon to oxygen is 1:1 in all the reactions, the oxygen input rate and the carbon consumption rate must be equal:

$$\sum_{k=1}^{3} V^{O}_{in,k}(t) = \sum_{k=1}^{3} V^{C}_{out,k}(t) \quad [8]$$

In this paper, it is assumed that the PC blown into the furnace is fully combusted in the raceway. In other words, the consumption rate of the carbon in PC is uniquely determined by the 1D transient model inputs:

$$V^{C}_{out,1}(t) = V^{PC}_{in}(t) \times X^{C}_{PC}/M_C/60 \quad [9]$$

where X^{C}_{PC} is the carbon content in PC, and M_C is the atomic weight of carbon. The 1D transient model also assumes that the moisture content reacts with carbon in the coke, *i.e.*, $V^{C}_{out,3}(t) = V^{O}_{in,3}(t)$. Using Eq. [8], the coke combustion rate in the raceway is calculated by:

$$V^{C}_{out,2}(t) = \sum_{k=1}^{2} V^{O}_{in,k}(t) - V^{C}_{out,1}(t) \quad [10]$$

where all the variables on the right-hand side are uniquely determined by $\boldsymbol{u}(t)$.

In the raceway, the hydrogen content in BM and PC turns into H_2 gas:

$$V^{H_2}_{in,1}(t) = V^{H_2}_{out,1}(t) = (BV(t) + BVO(t)) \times BM(t)/M_{H_2O}/1,000/60 \quad [11]$$

$$V^{H_2}_{in,2}(t) = V^{H_2}_{out,2}(t) = V^{PC}_{in}(t) \times X^{H}_{PC}/M_{H_2}/60 \quad [12]$$

where X^{H}_{PC} is the hydrogen content in the PC.

In the hearth region, SiO_2 contained in the slag is partially reduced by the carbon in the coke and this reaction also emits CO gas. The molar ratio of carbon to oxygen is 1:1 in this reaction.

$$V^{O}_{in,4}(t) = V^{C}_{out,4}(t) = 2R_{13} \quad [13]$$

2. *Carbon balance of coke*

The carbon balance derived from the coke in the entire furnace is discussed here. In addition to the carbon consumed by $R_i (i = 9, 10, 13)$ in the lower furnace, the coke carbon is consumed by $R_i (i = 5, 6, 7, 8)$ in the blast furnace. The reactions $R_i (i = 5, 6, 7)$ consume the coke carbon and emit CO gas, and the carbon consumption rate by these reactions is grouped as $V^{C}_{out,5}(t) = R_5 + R_6 + R_7$. Let $V^{C}_{out,6}(t) = R_8$ be the carbon consumption rate by the carburization reaction which does not generate CO gas. The coke carbon input rate from the top furnace is denoted as $V^{C}_{in}(t)$ (kmol/s):

$$V^{C}_{in}(t) = V^{Coke}_{in}(t) \times X^{C}_{Coke}/M_C/60 \quad [14]$$

where $V^{Coke}_{in}(t)$ is the coke loading rate (kg/min) from the top furnace and X^{C}_{Coke} is the carbon content in the coke.

The coke carbon consumption rate equals the coke carbon input rate at the steady state:

$$V^{C}_{in}(t) = \sum_{k=2}^{6} V^{C}_{out,k}(t) \quad [15]$$

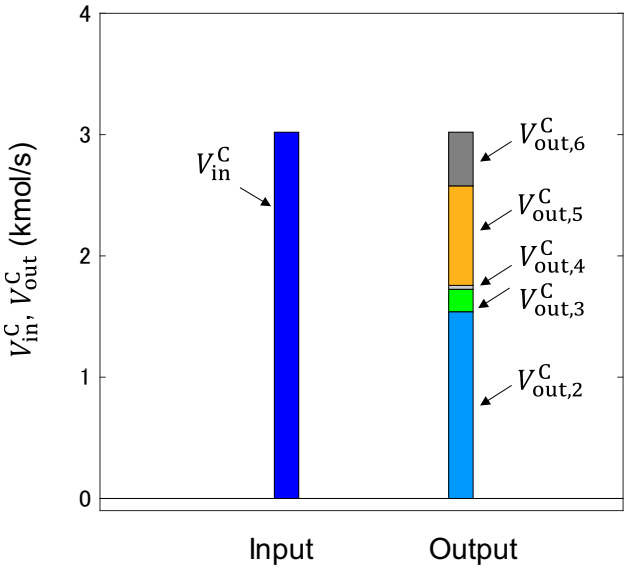

Fig. 6—Carbon balance of coke in entire furnace.

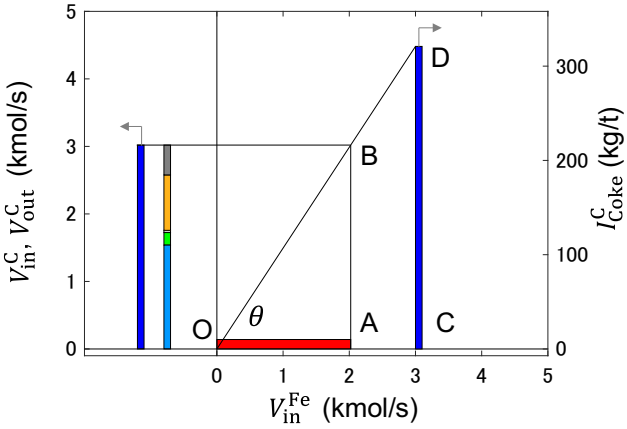

Fig. 7—Mechanism for determining production rate.

It should be noted, however, that this equation does not hold for the transient conditions, such as immediately after the CR change. The bar graphs in Figure 6 represent the supply and consumption rates of coke-derived carbon.

3. *Mechanism for determining production rate*

This section explains how the production rate is determined by the coke loading rate and the directly adjustable variable $CR(t)$. $CR(t)$ is defined by the ratio between the coke loading rate $V_{in}^{Coke}(t)$ and the production rate $Prod(t)$.

$$CR(t) = V_{in}^{Coke}(t)/Prod(t) \quad [16]$$

The molar iron input rate from the iron ore, $V_{in}^{Fe}(t)$, is proportional to $Prod(t)$:

$$V_{in}^{Fe}(t) = Prod(t)/M_{Fe} \times 1,000/60 \quad [17]$$

where M_{Fe} is the atomic weight of iron.

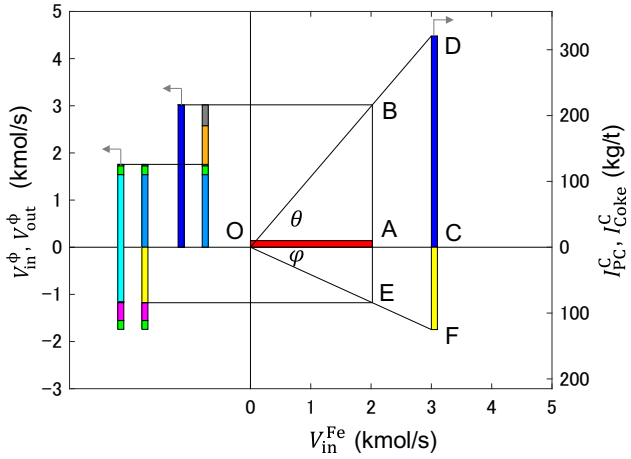

Fig. 8—Mechanism for determining carbon intensity. Superscript ϕ in left vertical axis denotes substances C, O, and H_2.

The coke carbon input rate $V_{in}^{C}(t)$ and iron input rate $V_{in}^{Fe}(t)$ can be linked with $CR(t)$ by combining Eqs. [14], [16], and [17]:

$$\begin{aligned} CR(t) \times X_{Coke}^{C} &= a \times V_{in}^{C}(t)/V_{in}^{Fe}(t) \\ &= V_{in}^{Coke}(t) \times X_{Coke}^{C}/Prod(t) \end{aligned} \quad [18]$$

where $a = 1,000 M_C/M_{Fe}$ is a constant of proportionality.

Figure 7 shows the relationship between the coke loading rate and the Prod based on Eq. [18]. To present the means to control the coke loading rate, the coke–carbon balance presented in Figure 6 is included in the graph. Here, the lengths of the segments $\overline{OA}$ and $\overline{AB}$ are $V_{in}^{Fe}(t)$ and $V_{in}^{C}(t)$, respectively, and the slope of $\overline{OB}$ is $\tan\theta = V_{in}^{C}(t)/V_{in}^{Fe}(t)$. By setting the length of $\overline{OC}$ to an arbitrary constant $b(= 3$ in Figure 7), the carbon intensity deriving from the coke $I_{Coke}^{C}(t) \equiv CR(t) \times X_{Coke}^{C}$, which is equal to $a\tan\theta$, can be represented by the length of $\overline{CD}$, which is measured by the right vertical axis. Increasing the coke loading rate and decreasing CR are effective to increase the Prod. Although the coke loading rate cannot be directly manipulated, it can be increased by increasing BV and the coke consumption rate in the raceway ($V_{out,2}^{C}(t)$).

4. *Mechanism for determining carbon intensity*

The carbon intensity is defined by the sum of coke-derived carbon intensity $I_{Coke}^{C}(t)$ and the PC-derived carbon intensity $I_{PC}^{C}(t) \equiv PCR(t) \times X_{PC}^{C}$:

$$\begin{aligned} I_C(t) &= I_{Coke}^{C}(t) + I_{PC}^{C}(t) \\ &= CR(t) \times X_{Coke}^{C} + PCR(t) \times X_{PC}^{C} \end{aligned} \quad [19]$$

where $PCR(t)$ stands for the amount of PC per iron.

$$PCR(t) = V_{in}^{PC}(t)/Prod(t) \quad [20]$$

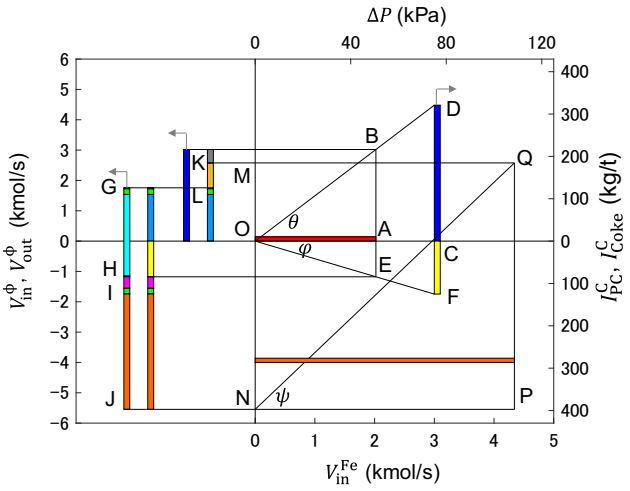

Fig. 9—Mechanism for determining the pressure drop. Superscript ϕ in left vertical axis denotes substances N_2, C, O, and H_2.

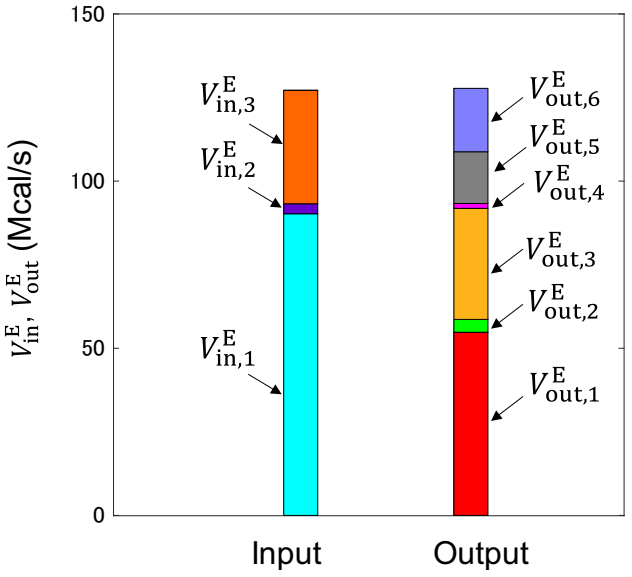

Fig. 10—Energy balance of entire furnace per second.

$I_{Coke}^{C}(t)$ is directly adjustable by changing CR, whereas $I_{PC}^{C}(t)$ is an operation result. Using Eqs. [9], [17], and [20], and the proportional constant a in Eq. [18], $I_{PC}^{C}(t)$ can be written by:

$$I_{PC}^{C}(t) = PCR(t) \times X_{PC}^{C} = a \times V_{out,1}^{C}(t)/V_{in}^{Fe}(t) \quad [21]$$

This relationship makes it possible to measure the carbon intensity derived from the PC and the coke by the same scale by taking the ratio between $V_{out,1}^{C}(t)$ and $V_{in}^{Fe}(t)$. The carbon intensity can be represented as:

$$I_{C}(t) = a \times \left(V_{in}^{C}(t) + V_{out,1}^{C}(t)\right)/V_{in}^{Fe}(t) \quad [22]$$

Figure 8 shows the mechanism for determining the carbon intensity. This figure is based on Figure 7, and it is combined with Figure 5 which shows the mass balance in the lower furnace. For the sake of the consistency with Figure 7, the mass balance in Figure 5 is moved downwards so that the elements of the carbon consumption rates $V_{out,k}^{C}(t)(k = 2, 3, 4)$ align with those in Figure 7. Since the length of $\overline{AE}$ is $V_{out,1}^{C}(t)$ and the slope of $\overline{OE}$ is $\tan\varphi = V_{out,1}^{C}(t)/V_{in}^{Fe}(t)$, the PC-derived carbon intensity $I_{PC}^{C}(t) \equiv PCR(t) \times X_{PC}^{C}$, which is equal to $a\tan\varphi$, can be measured by the length of $\overline{CF}$ with the right vertical axis in Figure 8. Therefore, the length of $\overline{DF}$ corresponds to the carbon intensity.

5. *Mechanism for determining pressure drop ΔP*

This section discusses the mechanism for determining the ΔP in the furnace. The ΔP is almost proportional to the gas flow rate $V_{top}(t)$ at the top furnace. The top gas consists of N_2, CO, CO_2, H_2, and H_2O.

The nitrogen content in the top gas comes entirely from the N_2 gas in the hot blast and it is not involved in any reactions in the furnace. The other four gas components originate from the CO and H_2 gases produced in the lower furnace and CO gas formed by $R_i(i = 5, 6, 7)$. These reducing gases are partially oxidized by R_2 and R_3 and turn into CO_2 and H_2O. The molar gas flow rate does not change by $R_i(i = 2, 3, 4)$. Therefore, the top gas flow rate can be expressed by:

$$V_{top}(t) = V_{out}^{N_2}(t) + \sum_{k=1}^{2} V_{out,k}^{H_2}(t) + \sum_{k=1}^{5} V_{out,k}^{C}(t) \quad [23]$$

where the molar flow rates of nitrogen through the tuyere and at the top furnace are $V_{in}^{N_2}(t) = V_{out}^{N_2}(t) = BV(t) \times 0.79/22.4/60$. Here, the H_2O gas derived from the water content of the raw material was not included in $V_{top}(t)$ because it is generated near the top furnace and has little effect on ΔP.

Figure 9 shows the mechanism for determining the ΔP, adding some elements to Figure 8. First, the nitrogen contained in the hot blast was added to the mass balance in the lower furnace, which is indicated by $\overline{IJ}$. The second term in Eq. [23] corresponds to the length of $\overline{HI}$, and the third term is the sum of the lengths of $\overline{GH}$ and $\overline{KL}$. Therefore, the top gas flow rate is equal to the length of $\overline{MN}$. The length of $\overline{NP}$ is set equal to the pressure drop $\Delta P(t)$, which is measured by the top horizontal axis. The slope of $\overline{NQ}$, *i.e.*, $\tan\psi = V_{top}(t)/\Delta P(t)$, means the gas permeability. This gas permeability is calculated by Ergun's equation in the 1D transient model as shown in Appendix.[34] It can be increased by increasing CR because coke layers have larger particles than iron ore layers. In other words, the slopes of $\overline{OD}$ and $\overline{NQ}$ are expected to move similarly when CR is changed.

6. *Energy balance*

This section describes the energy balance in the entire furnace. The bar graph of Figure 10 shows the energy balance per second. The energy input consists of the combustion heat of the coke and the PC in the raceway, the heat generated by the CO gas reduction reaction R_2,

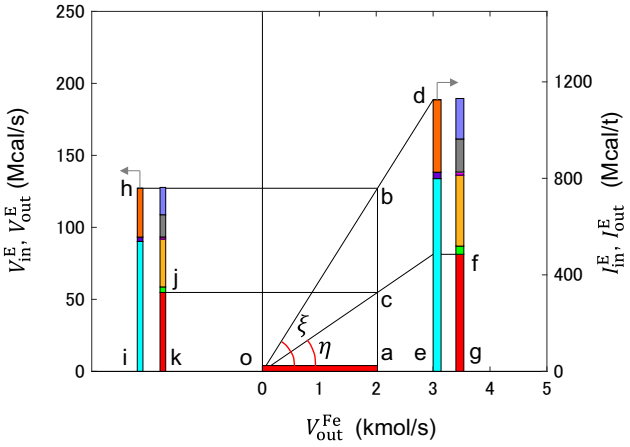

Fig. 11—Energy balance of entire furnace per unit amount of iron.

and the sensible heat of the nitrogen contained in the hot blast. These elements are denoted as $V^{E}_{in,k}(t)(k = 1, 2, 3)$, respectively.

$$V^{E}_{in,1}(t) = \Big(R_9\Delta H_{R_9} + R_{11}\Delta H_{R_{11}} + 0.5C_{p,O_2}V^{O}_{in,2}(t) \times BT(t)\Big)/4.18/1000 \quad [24]$$

$$V^{E}_{in,2}(t) = R_2\Delta H_{R_2}/4.18/1000 \quad [25]$$

$$V^{E}_{in,3}(t) = C_{p,N_2}V^{N_2}_{in}(t) \times BT(t)/4.18/1000 \quad [26]$$

where $C_{p,\phi}$ denotes the specific heat of gas component ϕ.

The energy output consists of the sensible heat of hot metal and slag, the decomposition heat of BM in the raceway (R_{10}), the heat absorption by the reaction $R_i(i = 5, 6, 7)$, the heat absorption by hydrogen gas reduction R_3, the heat loss from the furnace wall, and the other heats (gas shift reaction heat, water evaporation reaction heat, top gas sensible heat, and carburizing reaction heat), and these elements are denoted as $V^{E}_{out,k}(t)(k = 1, 2, \ldots, 6)$.

$$V^{E}_{out,1}(t) = \big(C_{p,Fe}V^{Fe}_{out}(t) + C_{p,Sl}V^{Sl}_{out}(t)\big) \times HMT(t)/4.18/1000 \quad [27]$$

$$V^{E}_{out,2}(t) = R_{10}\Delta H_{R_{10}}/4.18/1000 \quad [28]$$

$$V^{E}_{out,3}(t) = \sum_{k=5}^{7} R_k\Delta H_{R_k}/4.18/1000 \quad [29]$$

$$V^{E}_{out,4}(t) = R_4\Delta H_{R_4}/4.18/1000 \quad [30]$$

$$V^{E}_{out,5}(t) = q_{hl} \quad [31]$$

$$V^{E}_{out,6}(t) = \big(R_1\Delta H_{R_1} + R_4\Delta H_{R_4} + R_8\Delta H_{R_8} + C_{p,top}V_{top}(t) \times TGT(t)\big)/4.18/1000 \quad [32]$$

where $V^{Fe}_{out}(t)$ and $V^{Sl}_{out}(t)$ are melting rates of the hot metal and the slag, respectively, q_{hl} is the heat loss from the furnace wall, and $TGT(t)$ is the top gas temperature. $C_{p,Fe}$, $C_{p,Sl}$, and $C_{p,top}$ are the specific heat of the hot metal, the slag, and the top gas, respectively. While $V^{Fe}_{out}(t)$ is equal to $V^{Fe}_{in}(t)$ in the steady state, this is not generally the case in transient states.

Next, to convert energy per second to energy intensity per iron, Figure 11 normalizes the energy balance in Figure 10 by the iron melting rate $V^{Fe}_{out}(t)$, *i.e.*, $I^{E}_{in,k}(t) = V^{E}_{in,k}(t)/V^{Fe}_{out}(t) \times 1000/M_{Fe}(k = 1, 2, 3)$ and $I^{E}_{out,k}(t) = V^{E}_{out,k}(t)/V^{Fe}_{out}(t) \times 1000/M_{Fe}(k = 1, 2, \ldots, 6)$. First, the length of $\overline{oa}$ is set to $V^{Fe}_{out}(t)$. Then, the length of $\overline{ab}$ is set to the energy input rate per second, *i.e.*, $\sum_{k=1}^{3} V^{E}_{in,k}(t)$, and the length of $\overline{ac}$ is the energy output rate by the sensible heat of hot metal and slag, *i.e.*, $V^{E}_{out,1}(t)$. The slope of $\overline{ob}$ is $\tan\xi = \sum_{k=1}^{3} V^{E}_{in,k}(t)/V^{Fe}_{out}(t)$, and it is proportional to the total energy intensity per iron $I^{E}_{in}(t) \equiv \sum_{k=1}^{3} I^{E}_{in,k}(t)$. The slope of $\overline{oc}$, *i.e.*, $\tan\eta = V^{E}_{out,1}(t)/V^{Fe}_{out}(t)$, represents the sensible heat of hot metal and slag per iron $I^{E}_{out,1}(t)$, which is approximately proportional to HMT assuming that the slag rate, *i.e.*, $V^{Sl}_{out}(t)/V^{Fe}_{out}(t)$, is nearly constant. To ensure the consistency with Figure 9, the same constant b introduced in Figure 7 ($b = 3$) is used, and the lengths of $\overline{de}$ and $\overline{fg}$ are set to $b\tan\xi$ and $b\tan\eta$, respectively. $I^{E}_{in}(t)$ and $I^{E}_{out,1}(t)$ are measured by the right vertical axis in Figure 11.

7. *Integration of mass and energy balance*

Figure 12 integrates the mass balance in Figure 9 and the energy balance in Figure 11 in one diagram. This figure shows all the elements of means and ends in the BF operation in Figure 3 and the relationships between them. Moreover, the mass and energy balances per second and per iron which are highlighted in Figure 4 are clearly organized. In particular, the energy balance per iron and HMT are affected by the Prod, which is determined by the mass balance.

The manipulated variables can directly affect the following elements in the mass and energy balance. Increasing BV proportionally increases the lengths of $\overline{GH}$ and $\overline{IJ}$ in the mass balance, which represent the oxygen flow rate and the nitrogen flow rate, respectively. In addition, the lengths of the light blue and orange elements included in $\overline{hi}$ in the energy balance increase, showing the increase of the carbon combustion heat at the raceway and the sensible heat of the hot blast.

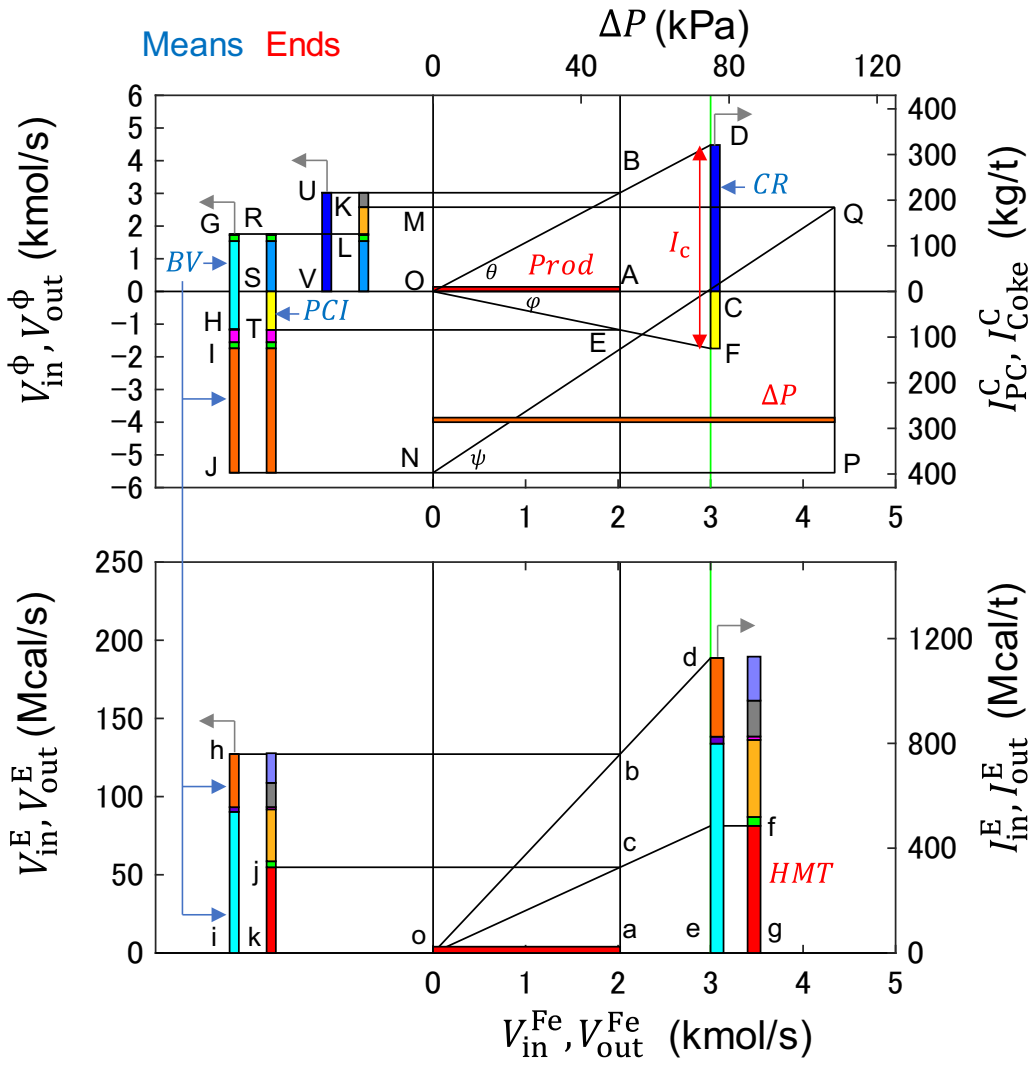

Fig. 12—Integration of mass and energy balance of BF process.

Increasing PCI increases the length of $\overline{ST}$, which indicates the PC flow rate. Finally, increasing CR increases the length of $\overline{CD}$, which represents the coke-derived carbon intensity.

Concerning the controlled variables, the Prod, the carbon intensity, HMT, and ΔP are represented by the lengths of $\overline{OA}$, $\overline{DF}$, $\overline{fg}$, and $\overline{NP}$. How these variables are affected by the manipulated variables is discussed in Section III-C.

C. *Means and Ends Relationships Based on Mass and Energy Balance*

This section presents the results of the control actions, such as changes in Prod and HMT, together with the changes in the mass and energy balance that occur in the BF. In the real blast furnace operation, the operation amounts of CR, PCI, and BV range from 5 to 20 kg/t, 10 to 80 g/Nm^3-O_2, 100 to 300 Nm^3/min, respectively.[5] The manipulated variables were changed based on these values.

1. *Step response to BV increase*

The standard operating condition shown in Table II was fed to the 1D transient model until the steady state was achieved. The step responses of the controlled variables, when BV was increased by 200 Nm^3/min, were then calculated.

Figures 13(a) and (b) show the manipulated variables (means) and the controlled variables (ends), respectively, and Figure 13(c) shows the mass and energy balance. The origin of the horizontal axes in Figures 13(a) and (b) indicates the moment when BV was increased. Small fluctuation of the controlled variables is caused by discontinuous burden descent in the 1D transient model, and it is observed even at the steady state.[24,25] For each bar of the mass and energy balance in Figure 12, both the current state and the future state 30 h after the BV

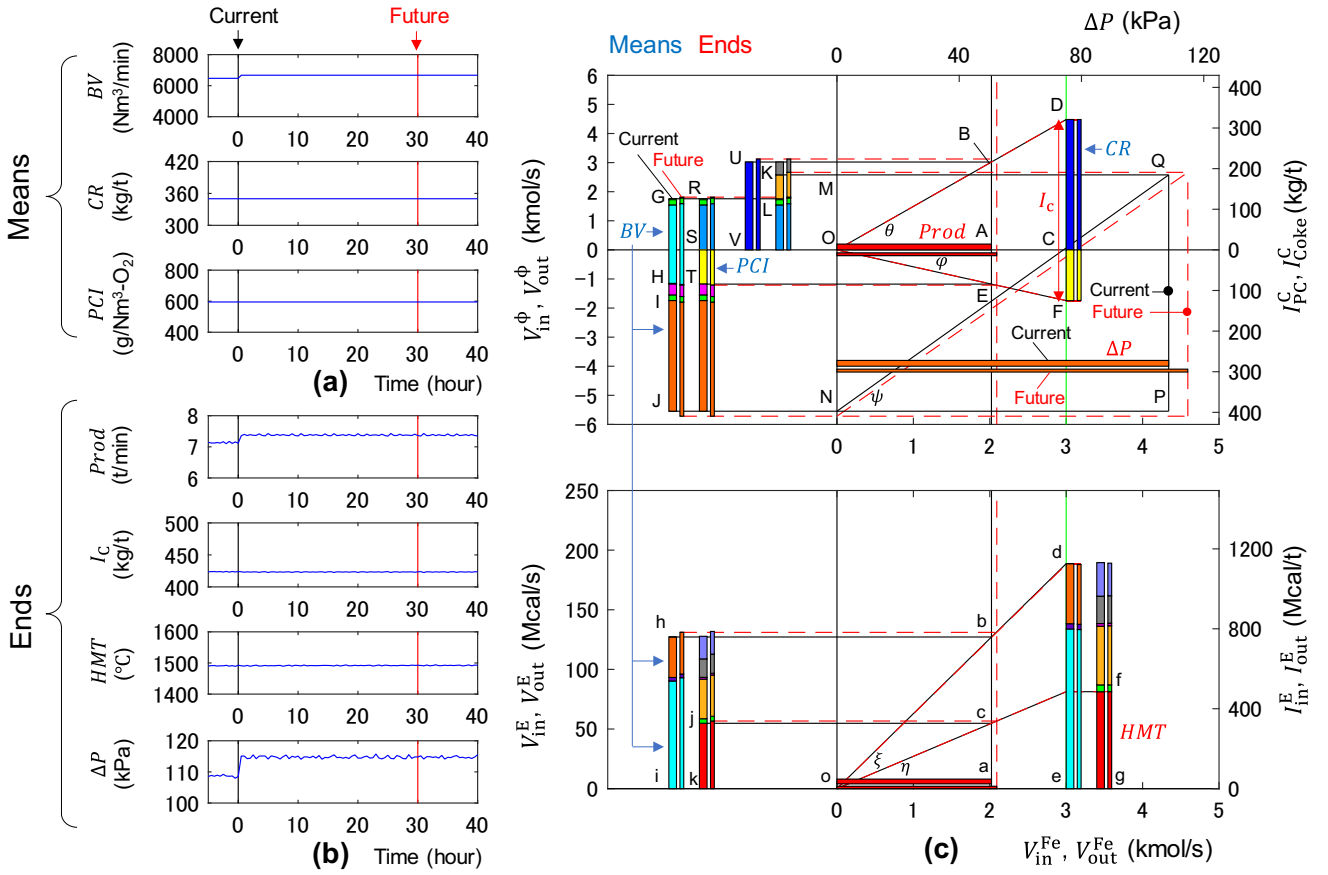

Fig. 13—Step responses of controlled variables and changes in mass and energy balance when BV is increased: (*a*) manipulated variables (means), (*b*) controlled variables (ends), and (*c*) mass and energy balance.

increase are shown in Figure 13(c). The thick bar and thin bar of each pair of bars represent the current state and the future state, respectively, which are indicated by the black and red vertical lines in Figures 13(a) and (b). Figure 13(b) shows that Prod and ΔP increase, whereas the carbon intensity and HMT remain almost constant with the BV increase. The mechanism behind these results is discussed using the mass and energy balance.

The mechanism of the Prod increase shown in Figure 13(b) is as follows. The changes in the mass balance in Figure 13(c) show that increasing the BV leads to an increase in the oxygen supply rate (length of $\overline{GH}$). The increased oxygen supply rate increases the coke carbon consumption rate in the raceway (length of $\overline{RS}$), causing the coke loading rate (length of $\overline{UV}$ = length of $\overline{AB}$) to increase. Since the CR is not manipulated, the length of $\overline{CD}$ and the slope of $\overline{OB}$ ($\tan\theta$) are fixed and the Prod (length of $\overline{OA}$) increases in proportion to the coke loading rate. When we pay attention to the triangle ΔOAB, this relationship can be clearly understood.

Concerning the carbon intensity (length of $\overline{DF}$ in Figure 13(c)), the coke-derived carbon intensity (length of $\overline{CD}$) does not change because the CR is not manipulated. The PC-derived carbon intensity (length of $\overline{CF}$) is determined by the slope of $\overline{OE}$ ($\tan\varphi$), which is the ratio of the PC flow rate (length of $\overline{AE}$ = length of $\overline{ST}$) to Prod (length of $\overline{OA}$). Since the PC flow rate increases in proportion to BV by Eq. [6] and Prod also increases, the slope of $\overline{OE}$ is almost constant. Therefore, the influence of BV increase on the carbon intensity is negligibly small as shown in Figure 13(b).

The energy balance in Figure 13(c) indicates that increasing the BV causes an increase in the total energy input rate per second (length of $\overline{hi}$ = length of $\overline{ab}$) and the energy output rate of the sensible heat of the hot metal and slag (length of $\overline{jk}$ = length of $\overline{ac}$). The intensities of the total energy input (length of $\overline{de}$) and the sensible heat of the hot metal and slag (length of $\overline{fg}$) per iron are determined by the slopes of $\overline{ob}$ and $\overline{oc}$ ($\tan\xi$ and $\tan\eta$), respectively. These slopes are almost constant because the iron melting rate in the lower furnace (length of $\overline{oa}$) also increases in proportion to BV. As a result, HMT in Figure 13(b) is unaffected by the BV increase.

Since the BV increase leads to the increased top gas flow rate (length of $\overline{MN}$ = length of $\overline{PQ}$) and the gas permeability corresponding to the slope of $\overline{NQ}$ ($\tan\psi$) is almost constant, the ΔP (length of $\overline{NP}$) increases in proportion to the BV, and this explains the increase of ΔP in Figure 13(c).

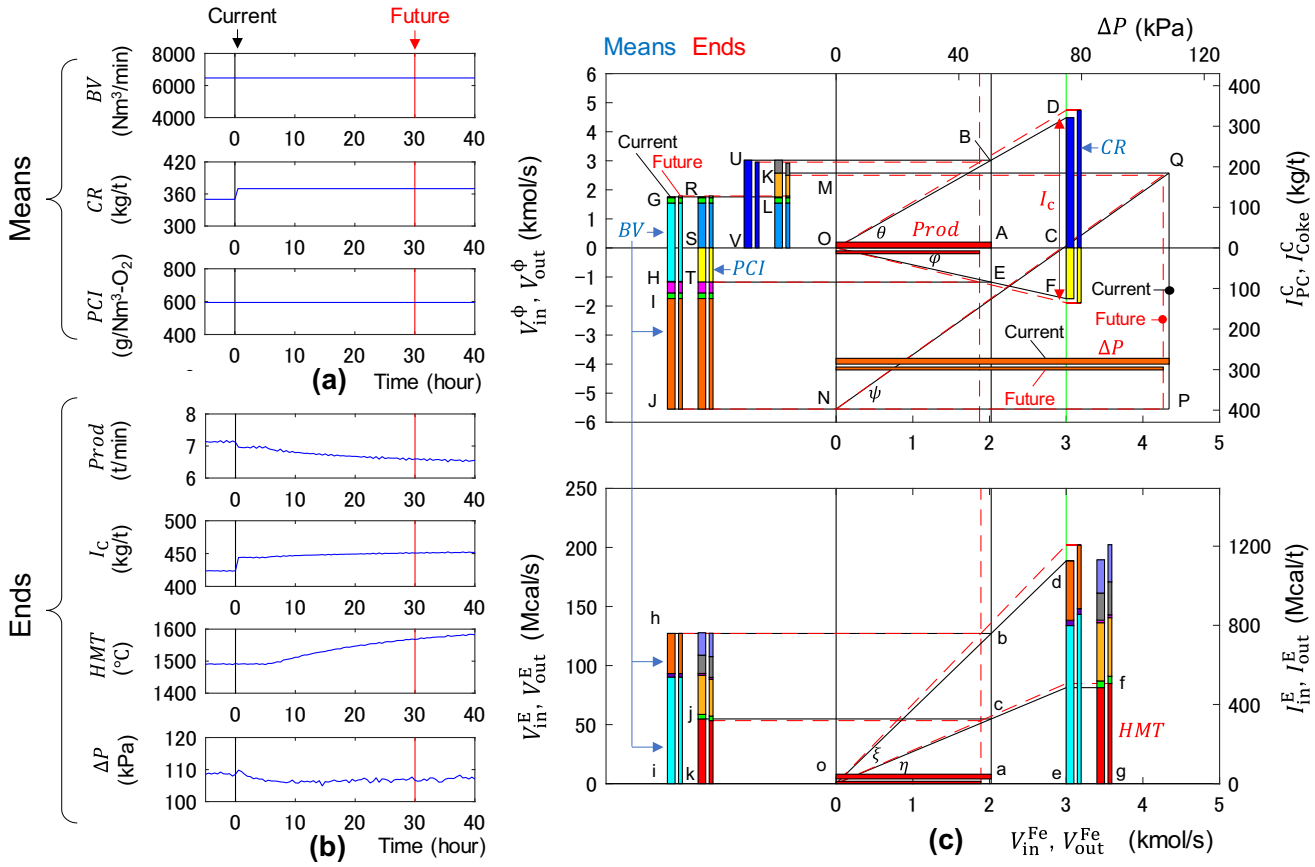

Fig. 14—Step responses of controlled variables and changes in mass and energy balance when CR is increased: (*a*) manipulated variables (means), (*b*) controlled variables (ends), and (*c*) mass and energy balance.

2. *Step response to CR increase*

Figure 14 shows the calculation result of the step responses of the controlled variables and the changes in mass and energy balance when the CR is increased by 20 kg/t. Figure 14(b) shows that Prod decreases, the carbon intensity increases, and ΔP decreases. HMT increases after about six hours of dead time due to the material's traveling time.

Figure 14(c) shows that increasing the CR increases the length of $\overline{\mathrm{CD}}$ and the slope of $\overline{\mathrm{OB}}(\tan\theta)$. The coke loading rate (length of $\overline{\mathrm{UV}}$ = length of $\overline{\mathrm{AB}}$) does not change significantly. Therefore, the Prod (length of $\overline{\mathrm{OA}}$) decreases, which explains the trend of Prod in Figure 14(b).

The increase in CR directly increases the coke-derived carbon intensity (length of $\overline{\mathrm{CD}}$). In addition, under the condition of constant PC flow rate (length of $\overline{\mathrm{ST}}$ = length of $\overline{\mathrm{AE}}$), the slope of $\overline{\mathrm{OE}}$ ($\tan\varphi$) increases due to the decrease in Prod (length of $\overline{\mathrm{OA}}$). Therefore, the PC-derived carbon intensity (length of $\overline{\mathrm{CF}}$) also increases. The carbon intensity in Figure 14(b) increases due to these two effects.

The decrease in Prod, *i.e.*, the iron input rate, leads to a reduction in the iron melting rate (length of $\overline{\mathrm{oa}}$) shown in Figure 14(c). Since BV is not manipulated, the energy input rate per second (length of $\overline{\mathrm{hi}}$ = length of $\overline{\mathrm{ab}}$) is almost unchanged. Hence, the slope of $\overline{\mathrm{ob}}$ ($\tan\xi$) and the intensity of the energy input (length of $\overline{\mathrm{de}}$) increase. This increases the intensity of the sensible heat of the hot metal and slag (length of $\overline{\mathrm{fg}}$). Thus, the HMT increase in Figure 14(b) can be explained by the increase in the energy input intensity per iron due to the decrease in Prod.

An increase in the CR increases the gas permeability (the slope of $\overline{\mathrm{NQ}}$, *i.e.*, $\tan\psi$) because of the increased thickness of the coke layers with larger particles. However, as shown in Ergun's equation, the gas permeability is affected not only by the particle size but also by the density of the gas. The increase in the CR decreases the gas density because of the increase in the gas temperature, and it has the effect of decreasing the permeability. Due to these two opposite effects, the gas permeability slightly increases and ΔP decreases as shown in Figure 14(b).

3. *Step response to PCI increase*

Figure 15 shows the calculation result of the step responses when the PCI is increased by 80 g/Nm^3-O$_2$. Figure 15(b) indicates that Prod decreases, the carbon intensity increases, HMT increases, and ΔP increases slightly due to the increase of PCI.

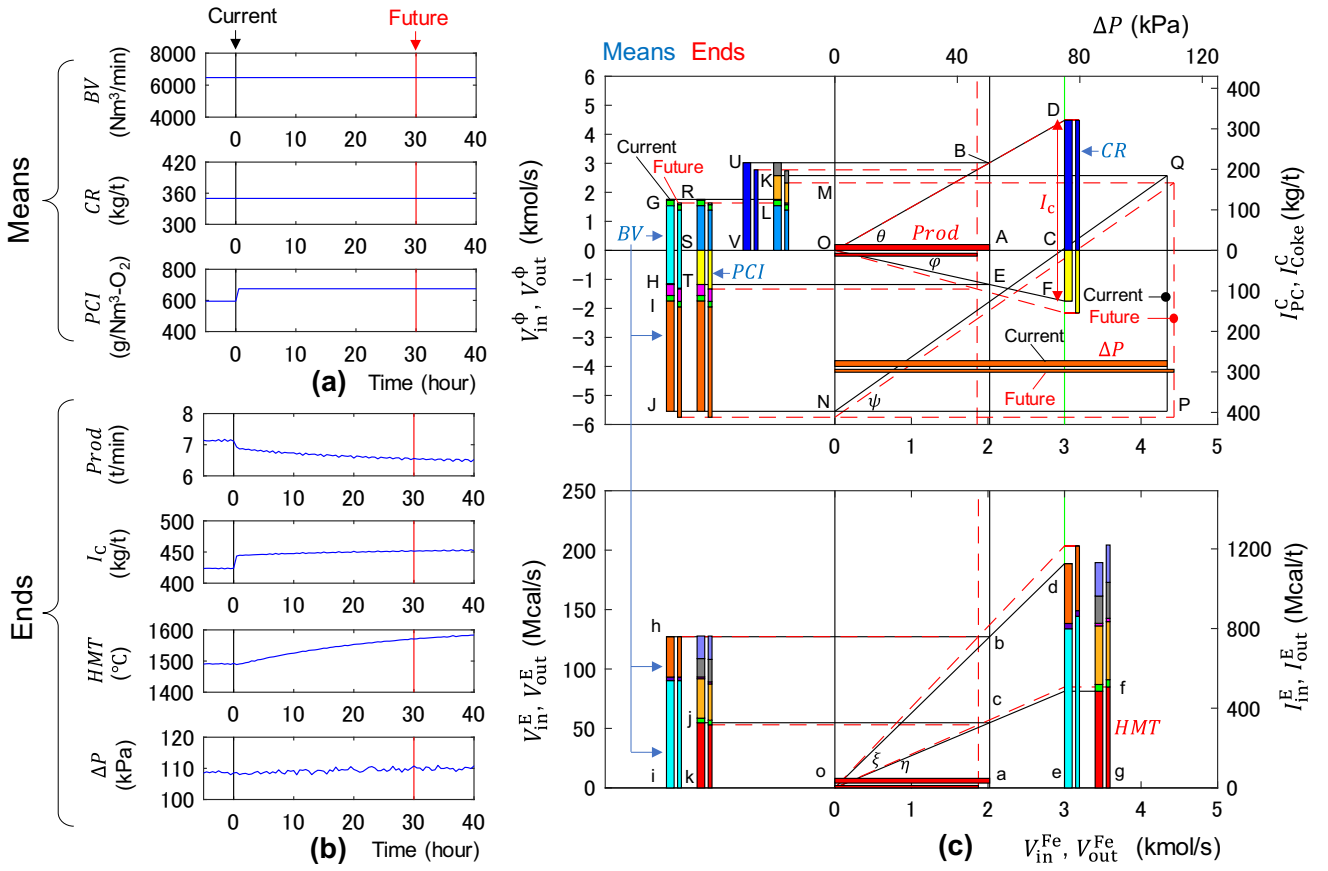

Fig. 15—Step responses of controlled variables and changes in mass and energy balance when PCI is increased: (*a*) manipulated variables (means), (*b*) controlled variables (ends), and (*c*) mass and energy balance.

Table IV. Operation Amounts of Manipulated Variables to Create Step-response Model

	$(\delta BV, \delta CR, \delta PCI)$		
	BV Response	CR Response	PCI Response
Large Increase	$(+200, 0, 0)$	$(0, +20, 0)$	$(0, 0, +80)$
Small Increase	$(+100, 0, 0)$	$(0, +10, 0)$	$(0, 0, +40)$
Small Decrease	$(-100, 0, 0)$	$(0, -10, 0)$	$(0, 0, -40)$
Large Decrease	$(-200, 0, 0)$	$(0, -20, 0)$	$(0, 0, -80)$

Figure 15(c) shows that increasing the PCI increases the consumption rate of PC carbon (length of $\overline{ST}$). Since the flow rate of oxygen supplied to the furnace is fixed due to the constant BV, the coke carbon consumption rate in the raceway (length of $\overline{RS}$) decreases. This results in a decrease in the coke loading rate (length of $\overline{UV}$ = length of $\overline{AB}$). Furthermore, since the slope of $\overline{OB}$, *i.e.*, $\tan\theta$, is fixed by the constant CR, the Prod (length of $\overline{OA}$) decreases in proportion to the coke loading rate. This is the mechanism of Prod decrease shown in Figure 15(b).

This decrease in the Prod (length of $\overline{OA}$) and the increase in the PC flow rate (length of $\overline{ST}$ = length of $\overline{AE}$) increase the slope of $\overline{OE}$ ($\tan\varphi$) and the PC-derived carbon intensity (length of $\overline{CF}$). The coke-derived carbon intensity (length of $\overline{CD}$) remains constant due to the constant CR. This is the mechanism of the carbon intensity increase in Figure 15(b).

The decrease in Prod also leads to the decrease in the iron melting rate (length of $\overline{oa}$) shown in Figure 15(c). Since the energy input rate per second (length of $\overline{hi}$) is almost constant, the slope of $\overline{ob}$ ($\tan\xi$) and the length of $\overline{de}$ increase, indicating that the intensity of the energy input per iron increases. Therefore, the length of $\overline{fg}$ corresponding to HMT also increases, which explains the HMT trend shown in Figure 15(b). Thus, the HMT increase by increasing PCI accompanies the reduction of Prod, as in the case of CR increase.

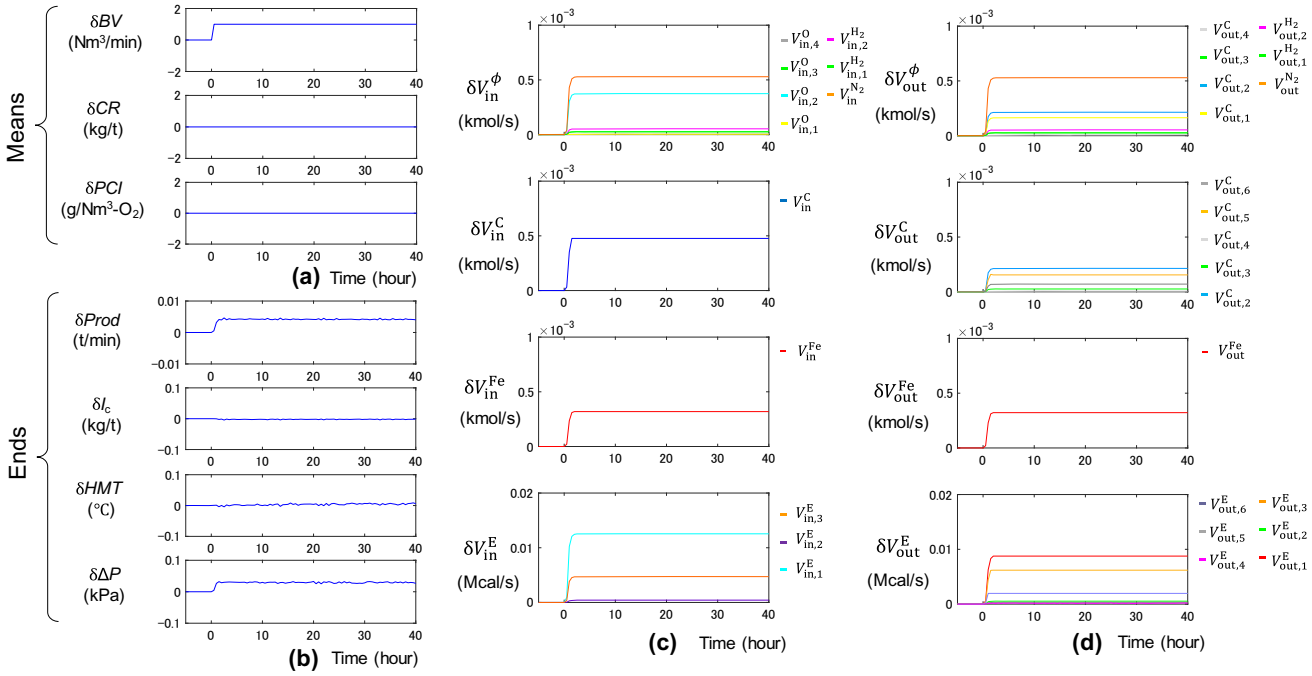

Fig. 16—Step responses of controlled variables and mass and energy flow rates to BV increase by unit amount: (*a*) manipulated variables (means), (*b*) controlled variables (ends), (*c*) mass/energy inflow rate, and (*d*) mass/energy outflow rate.

Figure 15(c) shows that the top gas flow rate (length of $\overline{MN}$) is not affected significantly when the PCI is increased. The gas permeability (slope of $\overline{NQ}$, *i.e.*, $\tan\psi$) decreases due to a reduction in gas density caused by the increase in the gas temperature. Other factors that can influence the gas permeability, such as coke particle size, remain constant. Therefore, ΔP increases slightly due to the increase of PCI as shown in Figure 15(b).

IV. ECOLOGICAL INTERFACE DESIGN

In this section, we develop an ecological interface that enables the operator to explore the appropriate control actions based on the internal mechanism of the process that links the means and ends described in Section III.

A. *What-If Analysis*

To enable the human operators to explore the appropriate control actions based on the calculation results of the 1D transient model in the real BF operation setting, it is necessary to predict and show the responses of all controlled variables when the operators virtually implement the control actions, hereafter referred to as what-if control actions, in real time. It is also desirable to show the changes in the mass and energy balance that link the means and the ends to enhance the situation awareness of the operators. Besides the 1D transient model in this study, numerous BF models considering complicated reactions and mass and heat transport phenomena have been developed.[33–38] However, the calculation speed to obtain the real-time solution has not been achieved. To address this issue, a step-response model is developed to reduce the computational load.

In Section III-C, the step responses of the controlled variables were calculated when each manipulated variable was increased under the steady-state operating conditions. In addition to these results, the step responses of the controlled variables were calculated not only in the direction of increasing each manipulated variable but also in the direction of decreasing it, *i.e.*, the four cases in each column of Table IV. In each case, the difference from the steady-state values before the manipulation was calculated and then normalized by the operation amount of each manipulated variable. The average of the four cases was then taken with respect to each manipulated variable. The step responses of all the elements regarding the mass and energy flow rates per second shown in Figure 12 were also calculated in the same manner.

As a representative result, Figure 16 shows the step responses of the controlled variables and the mass and energy flow rates to the BV increase by unit amount, where δ denotes the deviation from the steady state. Figure 16(a) shows the changes in the manipulated variables, and Figure 16(b) shows the changes in the

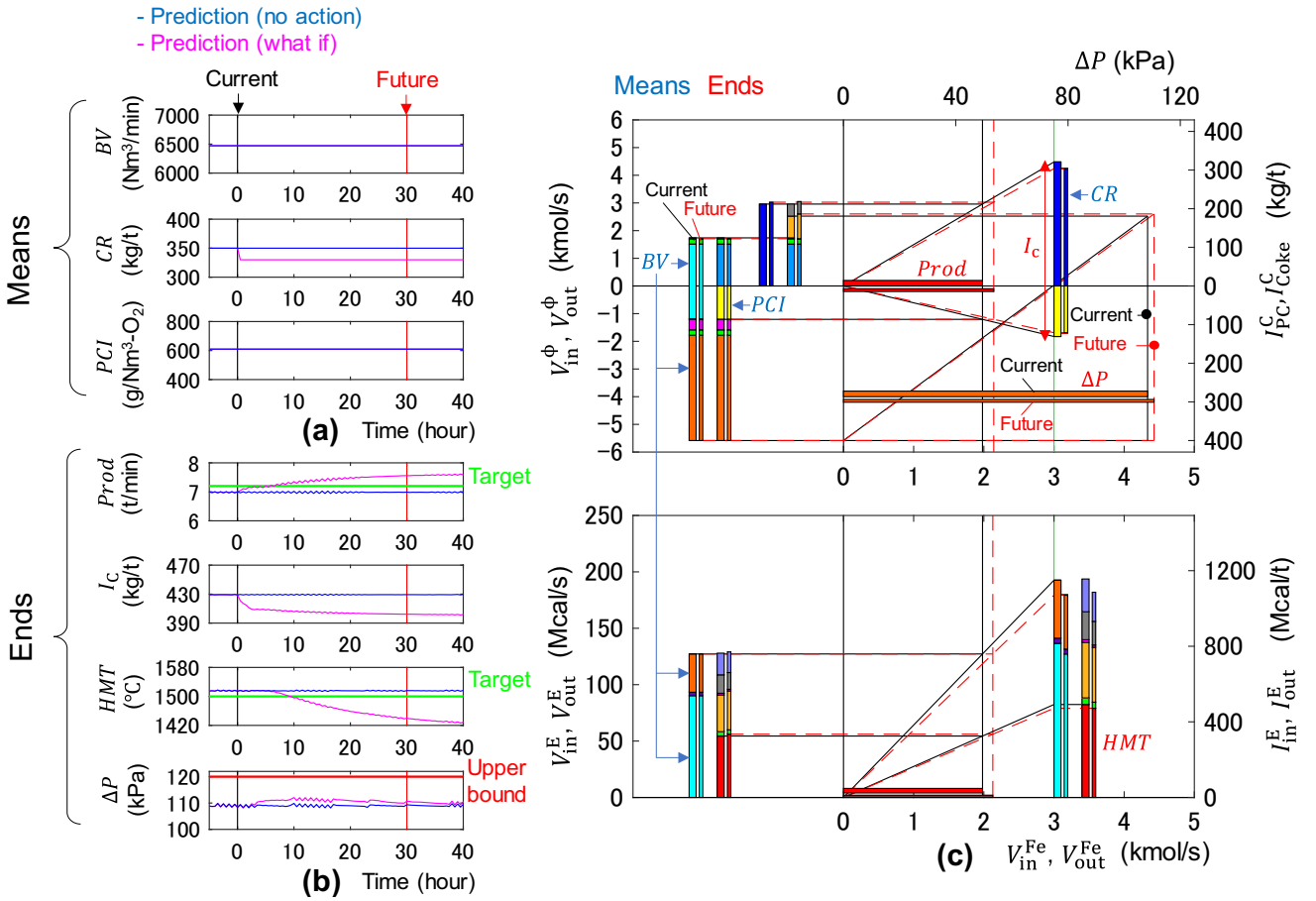

Fig. 17—Ecological interface based on what-if analysis: (*a*) manipulated variables (means), (*b*) controlled variables (ends), and (*c*) mass and energy balance.

controlled variables. Figures 16(c) and (d) show the mass/energy inflow rate and outflow rate, respectively. The first row in Figures 16(c) and (d) shows the elements of the mass balance in the lower furnace in Figure 5, and the second row shows the coke carbon balance in Figure 6. The third row shows the iron balance, *i.e.*, the iron input rate and the iron melting rate, and the bottom row shows the energy balance in Figure 10. In Figures 16(c) and (d), the line colors of the elements of the mass and energy balance are the same as the colors of the corresponding elements of the bar graphs in Figure 12.

These step responses allow the instantaneous prediction of the operation result when the what-if control actions are performed, consisting of possible combinations of the changes of BV, CR, and PCI. The future prediction of the controlled variables and the mass and energy flow rates at the current time step t_0 are approximated by the linear combination of the free response when no control action is taken and the step responses:

$$y_{j,\mathrm{wh}}(t_0+k) = y_{j,\mathrm{free}}(t_0+k) + \sum_{\tau=0}^{k}\sum_{i=1}^{3} S_{i,j}(k-\tau)\Delta m_i(\tau) \quad [33]$$

$$V^{\phi}_{*,\mathrm{wh}}(t_0+k) = V^{\phi}_{*,\mathrm{free}}(t_0+k) + \sum_{\tau=0}^{k}\sum_{i=1}^{3} S^{\phi}_{i,*}(k-\tau)\Delta m_i(\tau)(* = \mathrm{in}, \mathrm{out}) \quad [34]$$

where the subscripts wh and free represent the what-if response when the what-if control actions are taken and the free response, respectively. To predict up to the forty-hour-ahead future, k takes the values from 0 to 80. The subscripts i and j denote the manipulated variables (1 = BV, 2 = CR, 3 = PCI) and controlled variables. The superscript ϕ stands for the substances (C, O, H_2, N_2, Fe) or the energy (E). $S_{i,j}(k)$ is the step-response coefficient of the j-th control variable to the i-th manipulated variable at the time step k. $S^{\phi}_{i,*}(k)(* = \mathrm{in}, \mathrm{out})$ is the changes in the flow rate of the substance or the energy ϕ to the i-th manipulated variable at time step k. The time series of $S_{1,j}(k)$ and $S^{\phi}_{1,*}(k)$ are shown in Figures 16(b) through (d), respectively. $\Delta m_i(\tau)$ is the operation amount of the i-th manipulated variable at time step $t_0+\tau$. The free responses on the right-hand sides of Eqs. [33] and [34] are predicted with Eqs. [1] and [2] by fixing the input

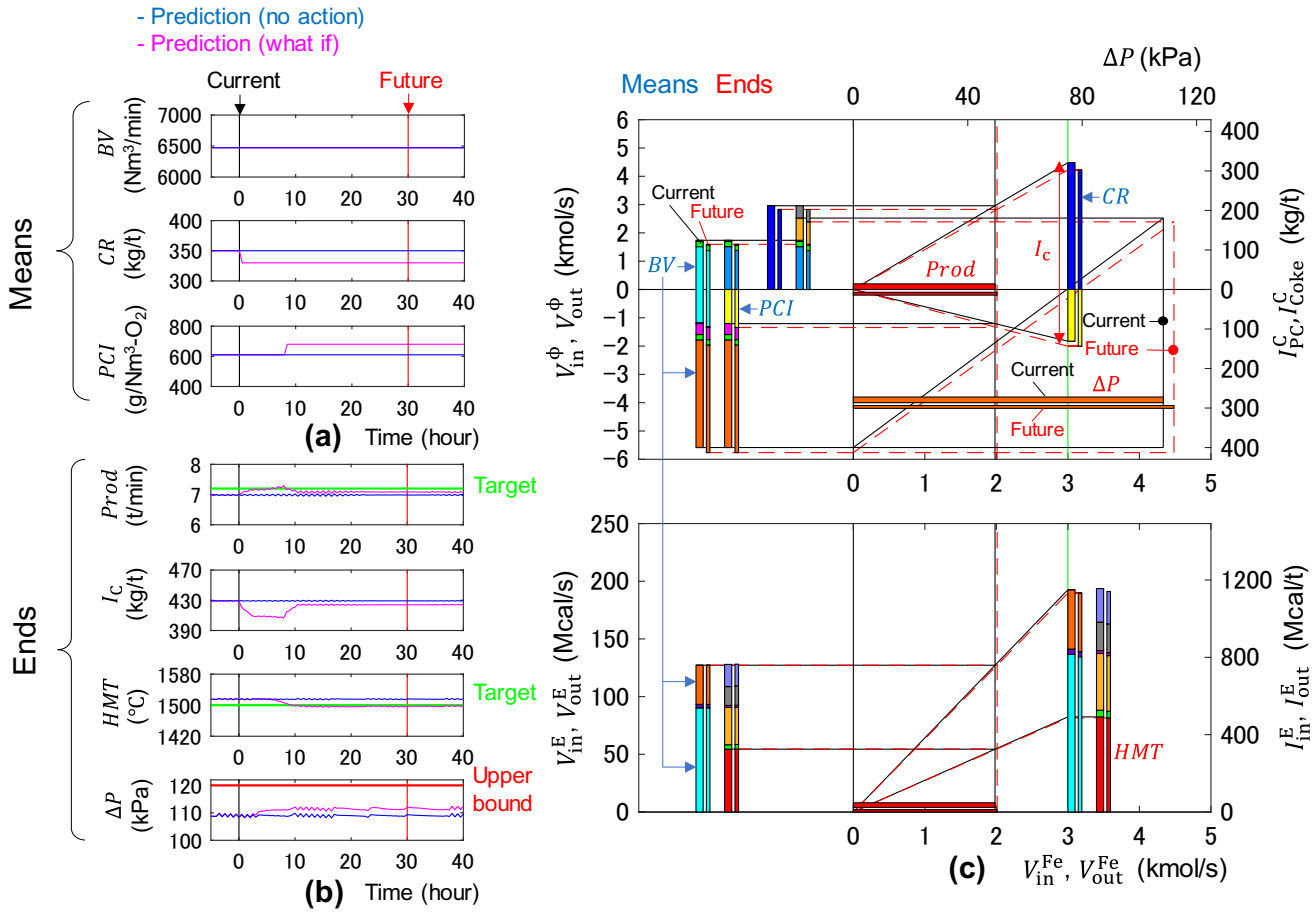

Fig. 18—Exploration of control actions using ecological interface (CR decrease and PCI increase): (*a*) manipulated variables (means), (*b*) controlled variables (ends), and (*c*) mass and energy balance.

variables, *i.e.*, $\boldsymbol{u}(t_0 + k) = \boldsymbol{u}(t_0)$. The real-time prediction of the free responses has already been achieved and successfully implemented in actual furnaces.[24]

B. *Ecological Interface Design*

Figure 17 shows the EI based on the what-if analysis described in Section IV-A. Figures 17(a) and (b) show the manipulated variables and controlled variables, where the origin of the horizontal axes is the current time. The blue lines in Figure 17(b) show the predicted free responses of the controlled variables when the manipulated variables are kept constant. The magenta lines in Figure 17(b) show the predicted what-if responses calculated by Eq. [24] when the what-if control actions shown by magenta lines in Figure 17(a) are taken. The green lines in Figure 17(b) show the target values of Prod and HMT, whereas the red line shows the upper bound of ΔP. Figure 17(c) shows the mass and energy balance, where the mass and energy flow rates are calculated by Eq. [25] and the carbon intensity and the energy intensity are calculated by the procedures described in Sections III-B-4 and III-B-6, respectively.

The following part demonstrates an example of the exploration process of appropriate control actions using the developed EI to achieve the control objectives. In this example, the current HMT is about 15 °C higher than the target and the current Prod is about 0.2 t/min lower than the target. Hence, CR is reduced by 20 kg/t as shown in Figure 17(a) to achieve the targets of HMT and Prod while reducing both the carbon intensity and the production cost. However, Figure 17(b) shows that the predicted what-if HMT is much lower than the target and the Prod is higher than the target due to the large magnitude of the manipulation.

To suppress the drop of HMT, Figure 18(a) explores the subsequent what-if control action, *i.e.*, increasing PCI by +70 g/Nm^3-O$_2$. Since it takes about six hours for HMT to start decreasing due to the traveling time of the material, the eight-hour-ahead PCI is increased to cope with the time delay. Figure 18(b) shows that this control action is expected to achieve the target HMT, while the carbon intensity is still maintained at a lower level than the current value. However, the increase in PCI causes the decrease in the coke loading rate and Prod, and the Prod is predicted to be still lower than the target.

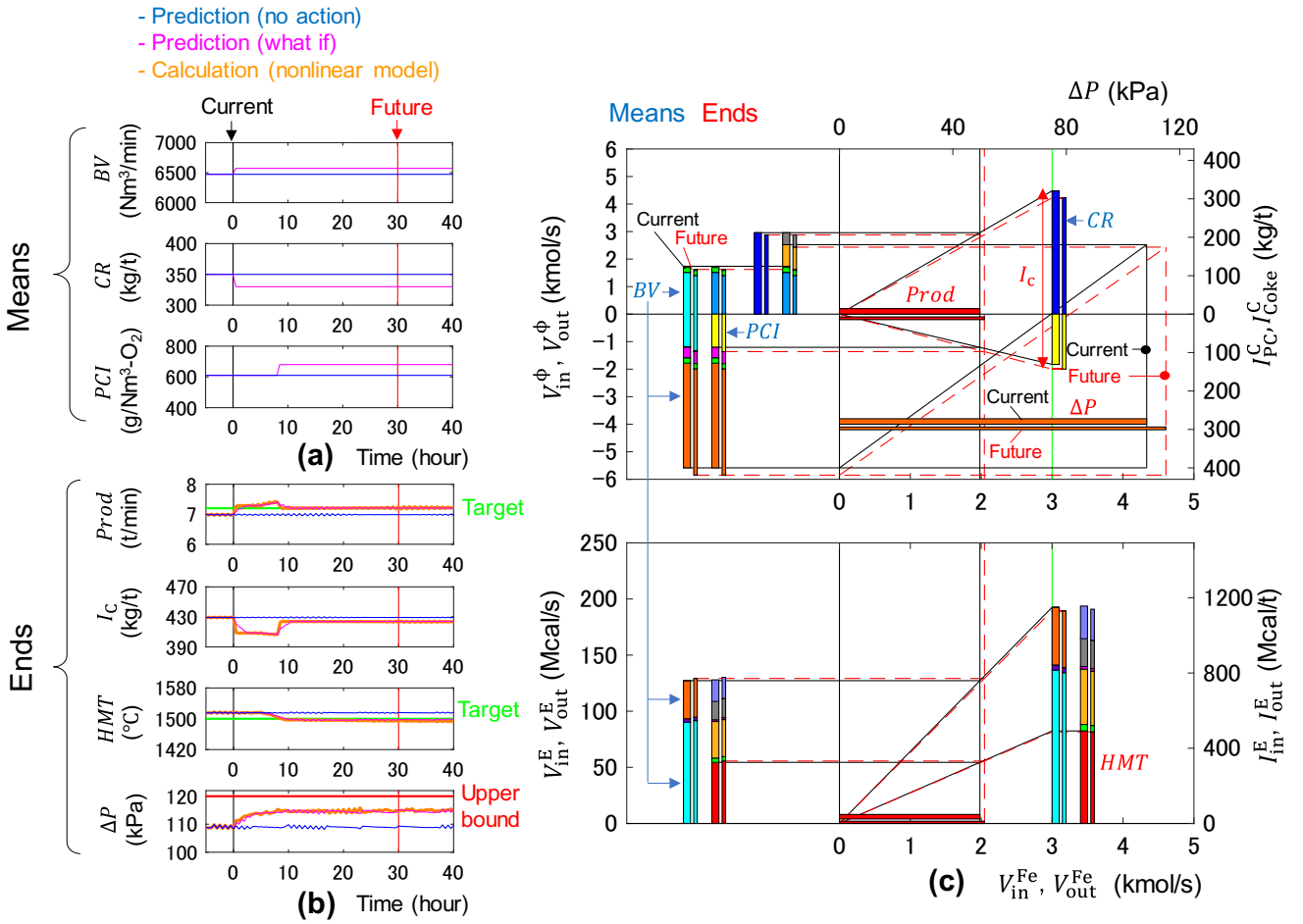

Fig. 19—Exploration of control actions using ecological interface (CR decrease, PCI increase, and BV increase): (*a*) manipulated variables (means), (*b*) controlled variables (ends), and (*c*) mass and energy balance.

To match the future Prod with the target value, Figure 19(a) explores the subsequent what-if action, to increase BV by 100 Nm^3/min. As a result, the oxygen flow rate from the tuyere and the coke combustion rate increase compared to Figure 18, causing the coke loading rate and Prod to increase. Figure 19(b) shows that the Prod is predicted to meet the target value and ΔP will increase, although it is still lower than the upper bound. The three control actions here are expected to bring the BF process to the desired new steady state.

The orange lines in Figure 19(b) show the calculation results using the 1D transient model when the explored control actions are executed. The magenta what-if lines agree well with the nonlinear 1D transient model calculation results, indicating the validity of the linearized step-response model. These results demonstrate that the EI was successfully developed to achieve the control objectives of maintaining HMT and Prod close to the target values while keeping ΔP below the upper bound and minimizing both the carbon intensity and the production costs. We plan to validate the effectiveness of the EI by incorporating it into a simulator and conducting experiments with human subjects.

C. *Future Work*

This section discusses the limitation of the developed EI and the issues to be overcome in future work. Firstly, the linear approximation with the step responses used in the what-if analysis may not be accurate when multiple manipulated variables are changed in larger operation amounts simultaneously. This is because some elements comprising the mass and energy balance are proportional to multiple manipulated variables; for example, Table III shows that $V^{C}_{out,1}$ is proportional to BV and PCI. Considering this nonlinearity explicitly in what-if analysis is future work. Secondly, to reduce the mismatch with actual operations, BM, BT, and EO, which were kept constant in this study, will be added to the manipulated variables, and the lower and upper constraints of the top gas temperature (TGT) and RAFT will be considered.

Ultimately, we plan to combine the developed EI and the existing automation system[5,6] to achieve human-centered automation. To apply the developed EI to actual operations, the estimation accuracy of the 1D transient model should be validated against the actual plant data. Although previous studies[24,25] have

confirmed the accuracy of HMT and Prod, the accuracy of ΔP has not yet been investigated. Since this 1D transient model is based on Ergun's equation, which cannot reproduce the radial and axial distributions of gas permeability in a real furnace, the 1D transient model needs to be improved by considering three-dimensional phenomena in the furnace. Sequential parameter modification, such as moving horizon estimation (MHE),[24] will be utilized to fit the model calculations to actual furnace data. This will incorporate the effects of unmeasurable disturbances, such as fluctuations in the material characteristics, into the model calculation. Furthermore, the representation of the mass and energy balance will be refined by incorporating operator feedback.

V. CONCLUSION

To realize an efficient and stable operation of the blast furnace (BF) in the steel industry, while retaining the proficient human operators' skills, a human–machine interface based on an ecological interface design (EID) was developed. The ecological interface (EI) presents predictions of the controlled variables when an operator performs hypothetical control actions based on a one-dimensional (1D) transient model. The mass and energy balance that links the manipulated variables and controlled variables, *i.e.*, the means–ends relationship, is also presented to raise the operators' situation awareness in the BF operation. The developed EI enables the operators to derive appropriate control actions that maintain hot metal temperature and production rate near the target values and keep the pressure drop below the upper bound while reducing carbon intensity and production costs. We will validate the effectiveness of the EI by incorporating it into a BF simulator and conducting experiments with human subjects.

CONFLICT OF INTEREST

On behalf of all authors, the corresponding author states that there is no conflict of interest.

OPEN ACCESS

This article is licensed under a Creative Commons Attribution-NonCommercial-NoDerivatives 4.0 International License, which permits any non-commercial use, sharing, distribution and reproduction in any medium or format, as long as you give appropriate credit to the original author(s) and the source, provide a link to the Creative Commons licence, and indicate if you modified the licensed material. You do not have permission under this licence to share adapted material derived from this article or parts of it. The images or other third party material in this article are included in the article's Creative Commons licence, unless indicated otherwise in a credit line to the material. If material is not included in the article's Creative Commons licence and your intended use is not permitted by statutory regulation or exceeds the permitted use, you will need to obtain permission directly from the copyright holder. To view a copy of this licence, visit http://creativecommons.org/licenses/by-nc-nd/4.0/.

APPENDIX

In the 1D transient model, the gas pressure P is calculated using Ergun's equation.[32]

$$-\nabla P = k_g \boldsymbol{u}_g \quad [35]$$

where $\boldsymbol{u}_g$ is the mass velocity of gas and k_g is the gas flow resistance.

$$k_g = \frac{150\mu(1-\varepsilon)^2}{\rho_g \varepsilon^3 (d_p \varphi)^2} + \frac{1.75(1-\varepsilon)|\boldsymbol{u}_g|}{\rho_g \varepsilon^3 (d_p \varphi)}. \quad [36]$$

where μ is the gas viscosity, d_p is the particle diameter, φ is the shape factor, ρ_g is the gas density, and ε is the voidage of the packed bed. The gas permeability in the main text is the inverse of k_g. It should be noted that Ergun's equation is a simplified calculation, and this work does not consider the degradation of the iron ore in the upper furnace and the percolation of iron ore particles into the coke layer.

ABBREVIATIONS

α	Proportionality constant
BM	Blast moisture (kg/m^3)
BT	Blast temperature (K)
BV	Blast volume (Nm^3/min)
BVO	Enrichment oxygen flow rate (Nm^3/min)
C_p	Specific heat (kJ/kmol/K)
CR	Coke rate (kg/t)
EO	Enrichment oxygen rate (pct)
HMT	Hot metal temperature (K)
I_C	Carbon intensity (kg/t)
I^C_{Coke}	Carbon intensity deriving from coke (kg/t)
I^C_{PC}	Carbon intensity deriving from PC (kg/t)
I^E	Energy intensity (Mcal/t)
M_ϕ	Atomic weight or molecular weight of substance ϕ (g/mol)
PCI	Pulverized coal injection rate (g/Nm^3)
PCR	Pulverized coal ratio (kg/t)
$Prod$	Production rate (t/min)
q_{hl}	Heat loss from the furnace wall (Mcal/s)
R	Reaction rate (kmol/s)
S	Step-response coefficient
$\boldsymbol{u}$	Input variables of nonlinear state-space model
V_{top}	Top gas flow rate (kmol/s)
V^{Coke}_{in}	Coke loading rate (kg/min)
V^{ϕ}_{in}	Inflow rate of substance ϕ (kmol/s)
V^{ϕ}_{out}	Outflow rate of substance ϕ (kmol/s)
V^E_{in}	Inflow rate of energy (Mcal/s)

$V_{\text{out}}^{\text{E}}$	Outflow rate of energy (Mcal/s)
$V_{\text{in}}^{\text{PC}}$	PC flow rate (kg/min)
$X_{\text{Coke}}^{\text{C}}$	Weight fraction of carbon in coke
X_{PC}^{ϕ}	Weight fraction of substance ϕ in PC
$\boldsymbol{x}$	State variables of nonlinear state-space model
$\boldsymbol{y}$	Output variables of nonlinear state-space model
Δm	Operation amount of manipulated variable
ΔP	Pressure drop (kPa)

REFERENCES

1. E. Mousa: *Metall. Mater. Eng.*, 2019, vol. 25, pp. 69–104.
2. M. Naito, K. Takeda, and Y. Matsui: *ISIJ Int.*, 2015, vol. 55, pp. 7–35. https://doi.org/10.2355/isijinternational.55.7.
3. P. Azadi, H. Elwan, R. Klock, and S. Engell: *J. Process. Control.*, 2023, vol. 129, p. 103032. https://doi.org/10.1016/j.jprocont.2023.103032.
4. Y. Hashimoto, R. Masuda, and S. Yasuhara: *ISIJ Int.*, 2022, vol. 62, pp. 157–64. https://doi.org/10.2355/isijinternational.ISIJINT-2021-073.
5. Y. Hashimoto, R. Masuda, M. Mulder, and M.M. van Paassen: *Metals*, 2022, vol. 12, p. 1624.
6. R. Masuda, Y. Hashimoto, M. Mulder, M.M. Van Paassen, and M. Kano: *Digit. Chem. Eng.*, 2023, vol. 7, p. 100085. https://doi.org/10.1016/j.dche.2023.100085.
7. U. Iffat, S. Bhatia, A. Tantar, J. Sanz, C. Schockaert, A. Schimtz, F. Giroldini, Y. Reuter, and F. Hansen: *IEEE 20th Conference on Business Informatics*, 2018, pp. 89–91. https://doi.org/10.1109/CBI.2018.10050.
8. Y. Hashimoto, Y. Okamoto, T. Kaise, Y. Sawa, and M. Kano: *ISIJ Int.*, 2019, vol. 59, pp. 1573–81. https://doi.org/10.2355/isijinternational.ISIJINT-2019-119.
9. P. Zhou, W. Chen, C. Yi, Z. Jiang, T. Yang, and T. Chai: *Eng. Appl. Artif. Intell.*, 2021, vol. 100, p. 104168. https://doi.org/10.1016/j.engappai.2021.104168.
10. P. Zhou, H. Song, H. Wang, and T. Chai: *IEEE Trans. Contr. Syst. Technol.*, 2017, vol. 25, pp. 1761–74. https://doi.org/10.1109/TCST.2016.2631124.
11. Y. Li, J. Zhang, Z. Liu, G. Wang, S. Li, and R. Wang: *Metall. Mater. Trans. B*, 2019, vol. 50, pp. 2296–2303. https://doi.org/10.1007/s11663-019-01628-7.
12. L. Jiao, X. Zhang, S. Kuang, and A. Yu: *Metall. Mater. Trans. B*, 2024, vol. 55B, pp. 3387–3406. https://doi.org/10.1007/s11663-024-03158-3.
13. K.J. Vicente and J. Rasmussen: *IEEE Trans. Syst, Man Cybern.*, 1992, vol. 22, pp. 589–606. https://doi.org/10.1109/21.156574.
14. K.J. Vicente: *Hum. Factors*, 2002, vol. 44, pp. 62–78. https://doi.org/10.1518/0018720024494829.
15. D.E. Howie and K.J. Vicente: *Int. J. Hum Comput Stud.*, 1998, vol. 49, pp. 651–74. https://doi.org/10.1006/ijhc.1998.0207.
16. J. Itoh, A. Sakuma, and K. Monta: *Control. Eng. Pract.*, 1995, vol. 3, pp. 231–39. https://doi.org/10.1016/0967-0661(94)00081-Q.
17. M.M. van Paassen, C. Borst, J. Ellerbroek, M. Mulder, and J.M. Flach: *IEEE Trans. Hum.-Mach. Syst.*, 2018, vol. 48, pp. 541–55. https://doi.org/10.1109/THMS.2018.2860601.
18. M.H.J. Amelink, M. Mulder, M.M. van Paassen, and J.M. Flach: *Int. J. Aviat. Psychol.*, 2005, vol. 15, pp. 205–31. https://doi.org/10.1207/s15327108ijap1503_1.
19. C. Borst, V.A. Bijsterbosch, M.M. van Paassen, and M. Mulder: *Cogn. Technol. Work*, 2017, vol. 19, pp. 545–60. https://doi.org/10.1007/s10111-017-0438-y.
20. G.A. Jamieson and K.J. Vicente: *Comput. Chem. Eng.*, 2001, vol. 25, pp. 1055–74. https://doi.org/10.1016/S0098-1354(01)00678-0.
21. G.A. Jamieson: *IEEE Trans. Syst. Man Cybern. Part A*, 2007, vol. 37, pp. 906–20. https://doi.org/10.1109/TSMCA.2007.897583.
22. C. Lindscheid, P. Sakthithasan, and S. Engell: *IFAC-PapersOnLine*, 2019, vol. 51, pp. 308–14. https://doi.org/10.1016/j.ifacol.2019.01.029.
23. X. Zhang, M. Kano, and S. Matsuzaki: *Comput. Chem. Eng.*, 2019, vol. 130, p. 106575. https://doi.org/10.1016/j.compchemeng.2019.106575.
24. Y. Hashimoto, Y. Sawa, and M. Kano: *ISIJ Int.*, 2019, vol. 59, pp. 1534–44. https://doi.org/10.2355/isijinternational.ISIJINT-2019-101.
25. Y. Hashimoto, Y. Kitamura, T. Ohashi, Y. Sawa, and M. Kano: *Control. Eng. Pract.*, 2019, vol. 82, pp. 130–41. https://doi.org/10.1016/j.conengprac.2018.10.009.
26. P. Azadi, J. Winz, E. Leo, R. Klock, and S. Engell: *Comput. Chem. Eng.*, 2022, vol. 156, p. 107573. https://doi.org/10.1016/j.compchemeng.2021.107573.
27. M. Yakeya, A. Kasai, R. Tadai, and K. Nozawa: *ISIJ Int.*, 2020, vol. 60, pp. 1438–44. https://doi.org/10.2355/isijinternational.ISIJINT-2019-699.
28. M. Geerdes, R. Chaigneau, O. Lingiardi, R. Molenaar, R. van Opbergen, Y. Sha, and P. Warren: *Modern Blast Furnace Ironmaking: An Introduction*, IOS Press, 2020, pp. 102–08.
29. K.J. Vicente: *Cognitive Work Analysis; Toward Safe, Productive, and Healthy Computer-Based Work*, 2nd ed. Lawrence Erlbaum Associates, Mahwah, 1999, pp. 149–79.
30. Y. Hashimoto, Y. Sawa, Y. Kitamura, T. Nishino, and M. Kano: *ISIJ Int.*, 2018, vol. 58, pp. 2210–18. https://doi.org/10.2355/isijinternational.ISIJINT-2018-177.
31. M. Jampani, J. Gibson, and P.C. Pistorius: *Metall. Mater. Trans. B*, 2019, vol. 50B, pp. 1290–99. https://doi.org/10.1007/s11663-019-01538-8.
32. Z. Zhao, X. Yu, and Y. Shen: *Fuel*, 2025, vol. 382, p. 133726. https://doi.org/10.1016/j.fuel.2024.133726.
33. D.M. Kundrat, T. Miwa, and A. Rist: *Metall. Trans. B*, 1991, vol. 22B, pp. 363–83. https://doi.org/10.1007/BF02651235.
34. S. Ergun: *Ind. Eng. Chem.*, 1953, vol. 45, pp. 477–85. https://doi.org/10.1021/ie50518a060.
35. P.B. Abhale, N.N. Viswanathan, and H. Saxén: *Miner. Process. Extract. Metall.*, 2020, vol. 129, pp. 166–83. https://doi.org/10.1080/25726641.2020.1733357.
36. S. Kuang, Z. Li, and A. Yu: *Steel Res. Int.*, 2018, vol. 89, p. 1700071. https://doi.org/10.1002/srin.201700071.
37. F. Bambauer, S. Wirtz, V. Scherer, and H. Bartusch: *Powder Technol.*, 2018, vol. 334, pp. 53–64. https://doi.org/10.1016/j.powtec.2018.04.062.
38. S. Natsui, M. Tanaka, A.S. Siahaan, and H. Nogami: *Metall. Mater. Trans. B*, 2022, vol. 53B, pp. 3842–55. https://doi.org/10.1007/s11663-022-02646-8.

Publisher's Note Springer Nature remains neutral with regard to jurisdictional claims in published maps and institutional affiliations.